# PIV MEASUREMENTS OF FLOW THROUGH FORMING FABRICS

by

Haiya Peng

B.Eng., Shanghai Jiao Tong University, P.R.China, 2007

A THESIS SUBMITTED IN PARTIAL FULFILLMENT OF

THE REQUIREMENTS FOR THE DEGREE OF

MASTER OF APPLIED SCIENCE

in

THE FACULTY OF GRADUATE STUDIES

(Mechanical Engineering)

THE UNIVERSITY OF BRITISH COLUMBIA

(Vancouver)

September 2011

## Abstract

Three-dimensional velocity fields in the single phase approach flow to a multiple layer woven forming fabric were measured using Particle Image Velocimetry (PIV). The measurements were conducted on a scale model of a forming fabric in a water/glycerin flow loop. Each strand on the paper side of the model forming fabric had a filament diameter around 15.4mm, and the loop test section was 310mm squared, permitting the measurement of detailed velocity distributions over multiple strands of the fabric. The flow speed in the loop test section were varied to achieve screen Reynolds numbers ($Re_s$), calculated based on paper side filament diameter (d), between 15 and 65. PIV measurements showed that the normalized ZD velocity deviation decreases from 19.7% at a plane 0.25d upstream from the forming fabric to 4.2% at a plane 1.5d upstream. The normalized CMD velocity deviation decreases from 15.3% at a plane 0.25d upstream from the forming fabric to 1.9% at a plane 1.5d upstream. The normalized MD velocity deviation decreases from 14.5% at a plane 0.25d upstream from the forming fabric to 2.3% at a plane 1.5d upstream. The highest ZD velocity is about 3.3 times higher than the lowest ZD velocity at a plane 0.25d above the fabric. This ratio decreases to 1.2 at a plane 1.5d above the fabric. These findings show that the flow non-uniformity caused by the fabric weave is restrained to a short distance above the fabric. However, even this non-uniformity is not particularly felt by fibers, whose length scale results in an averaging of the local velocity field. CFD simulations of the same flow were consistent with the PIV measurements.

## Preface

A version of chapter 2 has been published. Peng, H., Green, S.I., 2011. PIV Measurements of Flow Immediately above Woven Fabrics. TAPPI PAPERCON 2011, 2149-2157. Haiya Peng conducted the entire test and wrote all the manuscript. Sheldon I. Green's role was primarily supervisory.

Haiya Peng conducted all the experiments, simulations and analysis described in this thesis. Sheldon I. Green's role in the thesis was primarily supervisory; most of the intellectual content of the thesis is Haiya's.

# Table of Contents

## List of Figures

## Acknowledgements

I want to express my enduring gratitude to my supervisor Prof. Sheldon I. Green for his continuous guidance and exceptional patience during my research.

I would also like to thank my lab mates Ali Vakil, Seth Gilchrist, Jingmei Li and Purushotam Kumar for their help during the process of this project.

AstenJohnson Inc. and NSERC are gratefully acknowledged for their financial supports.

I want to thank Chu Lin for her personal support in the last two years.

Special thanks are owed to my beloved parents for their endless encouragement and financial support throughout my years of education.

# Chapter 1: Introduction

As one of the greatest inventions of ancient China, papermaking has played a significant role in the continuous progress of mankind. Paper has for a long time been the carrier of knowledge and history over generations. Today, paper is used to facilitate writing, printing, packaging, cleaning, and medicinal production, among other purposes. Global consumption of paper reaches approximately 400 million tons each year. The majority of this paper is used for printing and writing, which require paper sheets that possess a uniform density distribution. Methods for producing uniform paper are thus very important, and are the motivation of this thesis.

Papermaking involves three basic processes: forming, pressing and drying. At the forming stage, a dilute suspension of pulp in water, generally about 0.7% pulp by mass, is forced through a woven forming fabric, creating a pulp mat. In the process, fibers are filtered from the suspension as the water flows through the fabric, Adanur [1]. The fibrous mat is subsequently pressed and dried to create paper.

At the dewatering stage, the fibers in the pulp suspension follow the flow, and are distributed in a fashion that depends on the distribution of the velocity upstream from the forming fabric. It is known that the non-uniformity of the wet fibrous mat is difficult to change at subsequent stages, i.e. pressing and drying. Thus, the non-uniformity of the wet fibrous mat will have a profound effect on the structure of the printed end product, Danby [2] and Danby et al. [3]. This indicates that the velocity distribution of the flow upstream from forming fabric strongly affects the final paper quality. In this thesis, we use Particle Image Velocimetry (PIV) to

measure the detailed velocity distribution of the flow upstream from the forming fabric. We then investigate flow non-uniformity, and its possible effect on the fiber distribution.

In this chapter, we present a basic introduction of the papermaking process, followed by descriptions of the forming section, forming fabric, wire mark and PIV technique. A literature review is then followed by the thesis objective, approach and hypothesis.

## 1.1 Papermaking Process

The first authentic papermaking process originated from China as early as 105 AD. "The inventor Ts'ai Lun mixed a combination of rags, plant stems and wood ash and then boiled this in water. The resulting concoction was washed, thrashed and stirred in a large volume of water to break it down to pulp. A horsehair sieve (deckle) was dipped into the mixture and the water drained off leaving a layer of pulp. This was pressed flat, then dried and bleached naturally in the sun and the first sheet of paper was formed." [4].

The papermaking skill was kept a secret from the rest of the world until the middle of eighth century when it reached the Middle East, and then Europe in 1150. Paper mills functioned in Spain, Italy, Germany and France from the beginning of 15th century. Linen rags and cotton were the initial fiber sources for papermaking in Europe, and were replaced with ground wood pulp from the mid-19th century.

A number of significant inventions during the early 19th century provided the basis for the modern papermaking machine. Today, paper machines still follow the basic principles of Donkin's machine, in which the sheet is formed over a continuous wire at the wet end of the paper machine. The water is then drawn from the pulp in the press section of the machine by

squeezing the wet web between two press felts. The web is then run over a series of heated cylinders to evaporate remaining moisture [4].

As shown in Figure 1.1 [4], the modern papermaking process consists of the following steps: raw material preparation, e.g. debarking and chipping; pulp making; pulp bleaching; paper manufacturing and sheet converting. Given the focus of this research project, only paper manufacturing will be described at length.

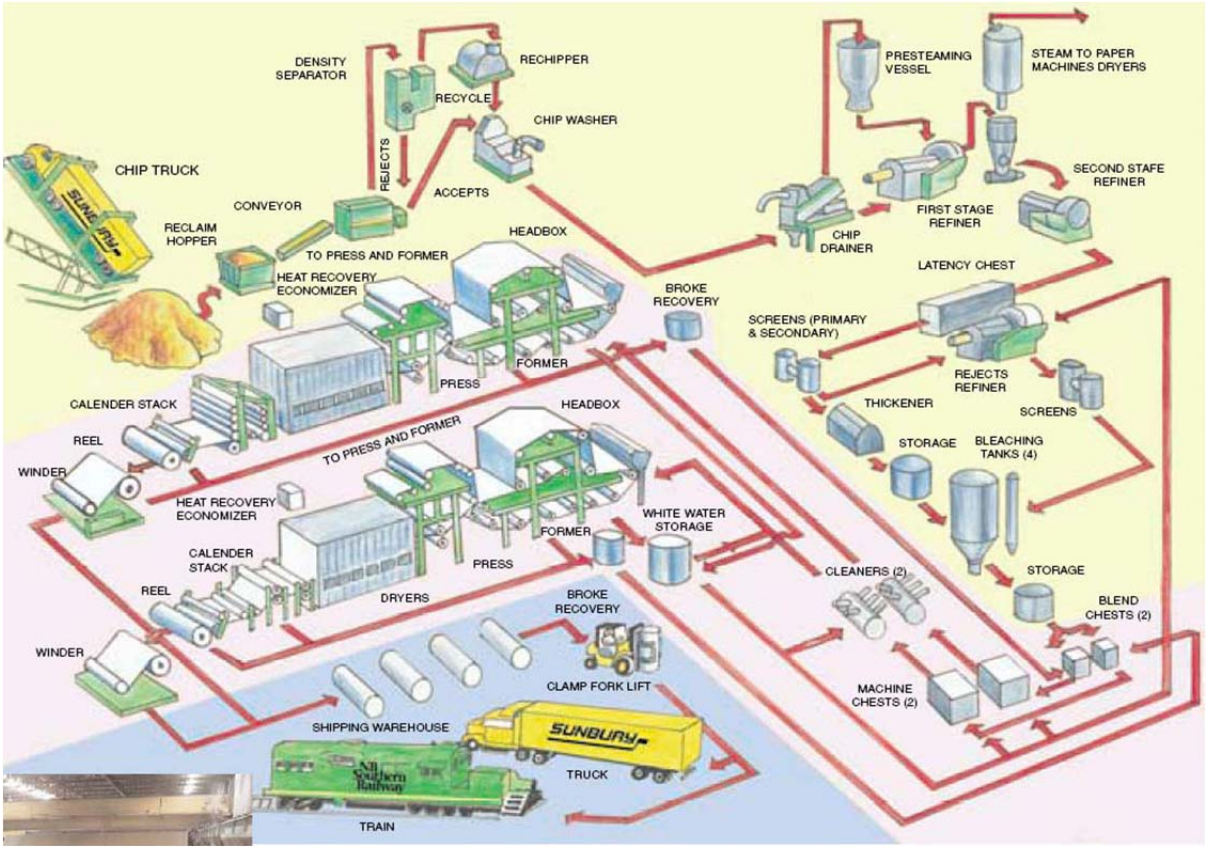


**Figure 1.1 Manufacturing process of pulp and paper**

Figure 1.2, courtesy to Paper machine Wikipedia, shows the four stages of the paper manufacturing process using a traditional Fourdrinier paper machine. At the forming stage, the 0.7% pulp suspension is sprayed from the headbox onto the surface of the forming fabric. The spray drains through the forming fabric to produce a wet pulp mat, producing a sheet

consistency of roughly 20%. At the pressing stage, the wet pulp mat is squeezed between rollers and press felts. This produces a sheet comprised of roughly 40% fiber and 60% water, depending on the sheet grade and the paper machine. At the drying stage, a heated dryer removes more water from the sheet, reducing the concentration of water in the finished paper sheet to 2-6%. Finally, at the calender stage, the paper is sent through a series of rollers, applying additional pressure and heat to the passing sheets. This procedure produces smoother, glossier and more uniform paper sheets.

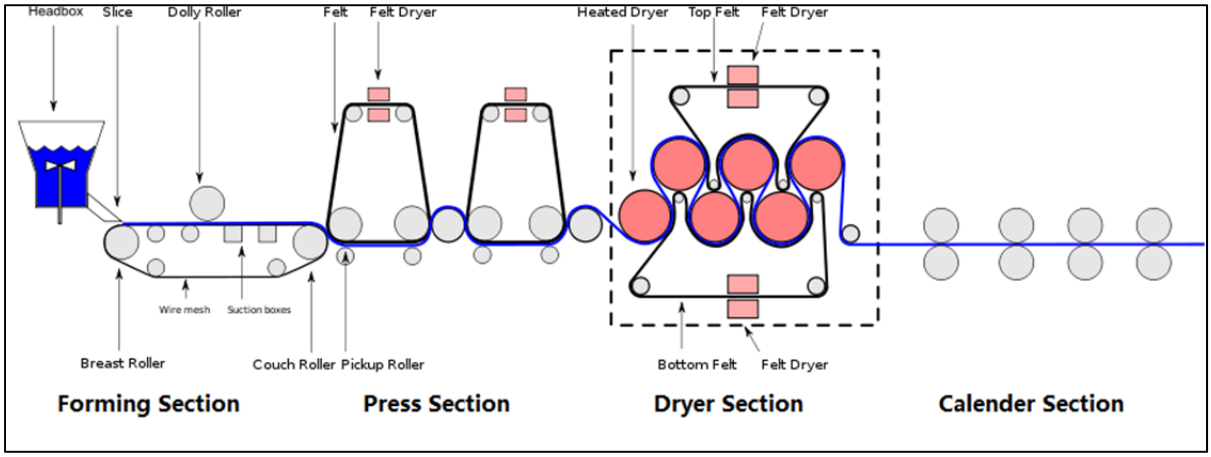


**Figure 1.2 Fourdrinier paper machine**

## 1.2 Forming Section

The forming process has the most influential effect on the surface quality of the finished paper sheet. Different forming methods will be discussed in this section.

The first high speed paper machine, the Fourdrinier machine, was invented in France by Louis Robert in 1799, and was later improved in Britain, where it was patented by Fourdrinier brothers. The major component of this machine is a moving endless belt of wire or plastic screen, which drains water from the pulp suspension and forms a continuous wet

sheet in the forming section, shown in Figure 1.3, courtesy to Henan Fuyuan Machinery Manufacturing Co., Ltd.

This endless belt of wire or plastic screen, now called the forming fabric, makes continuous and automatic production feasible, while dramatically increasing the speed of papermaking.

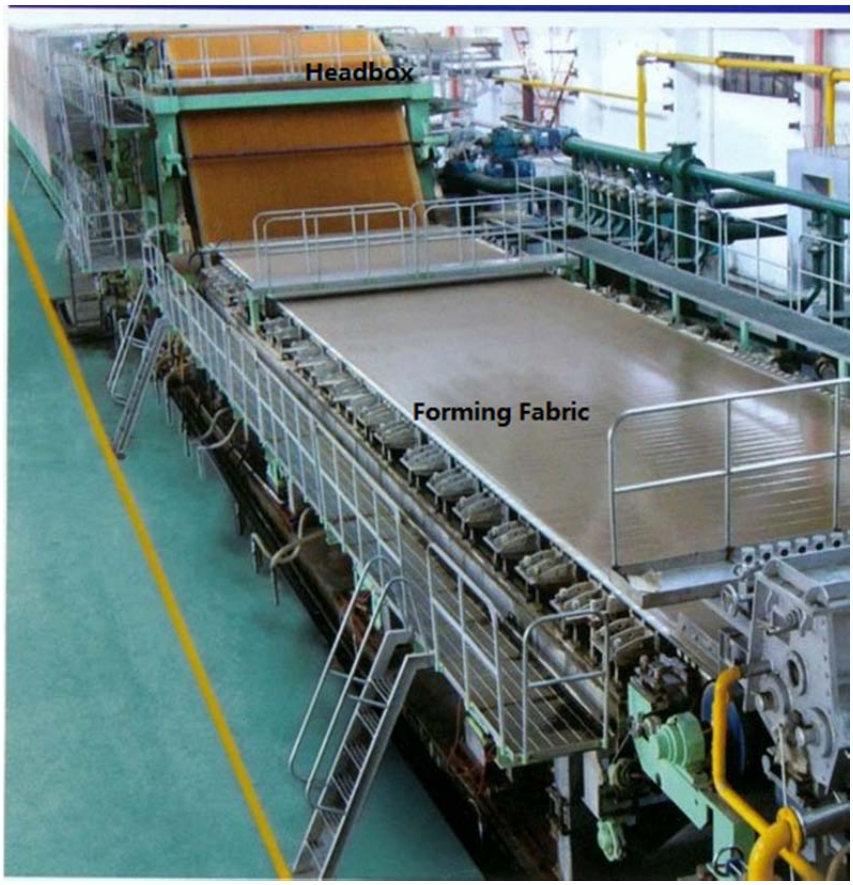


**Figure 1.3 Forming section of a modern Fourdrinier paper machine**

However, because the Fourdrinier machine only executes the drainage process in one direction, the two sides of the wet pulp mat formed from the forming section are not identical. Rather, the machine produces a pulp mat with two distinct sides: the wire side and felt side. The wire side is the side of a sheet or web of paper that has formed in contact with the papermaking machine's forming wire. The side formed over the top side of the paper is called the felt side. The felt side is usually smoother than the wire side since it does not touch

the wire of the paper machine. These distinct sides remain in the final paper sheet, which is undesirable. To eliminate this effect, a new twin wire former was developed. As shown in Figure 1.4 [5], a pulp suspension is sprayed into the gap between two forming fabrics, and the water drains through both fabrics to form a wet pulp mat with two identical sides.

Most other paper machine models, such as the top wire former and top Fourdrinier, use the same forming mechanism as the two machines mentioned above. To avoid redundancy, we will not elaborate on these models.

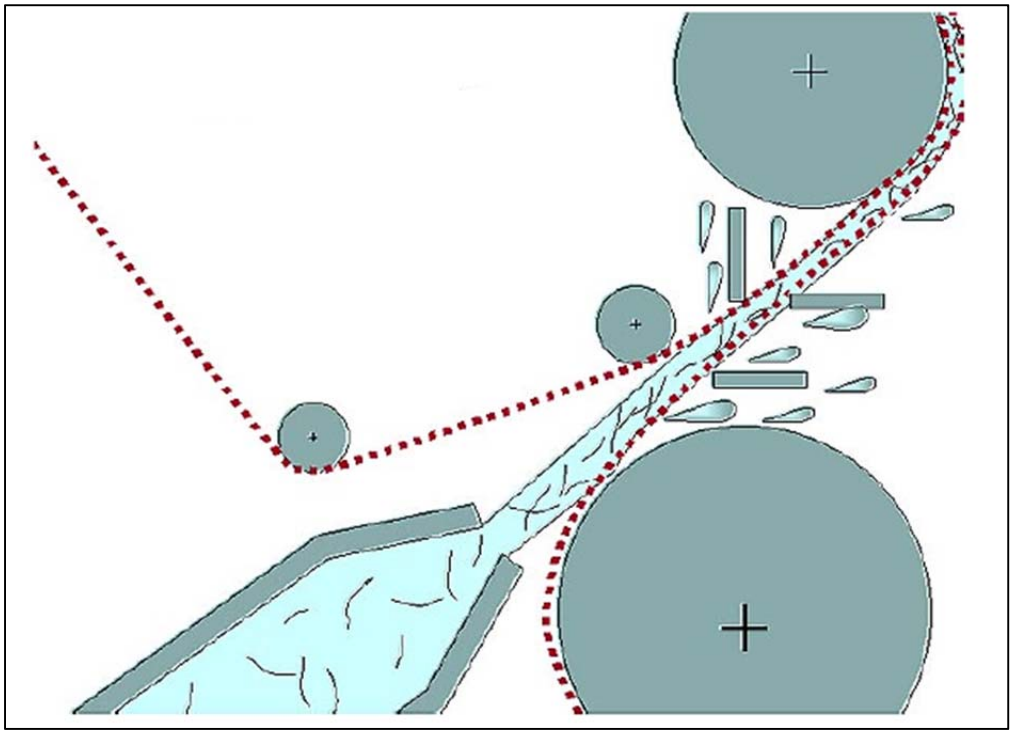

**Figure 1.4 Scheme of twin wire former**

## 1.3 Forming Fabric

As shown in Fig.2, forming fabrics, press fabrics and dryer fabrics are used in the papermaking process. Originally, the forming fabric was made of bronze wire and called the 'wire', and press and dryer fabrics were made from wool and cotton. Today, due to the

enhanced width and speed of paper machines, fabrics are made from synthetic fibers such as polyester and nylon, which are more durable and produce higher quality paper. Since our research focuses specifically on the velocity upstream from the forming fabric, we discuss only the forming fabric here.

The forming fabric structure is a complex three-dimensional woven matrix, which consists of machine direction (MD), and orthogonal cross machine direction (CMD) filaments in single or multiple layers. Figure 1.5, courtesy to AstenJohnson, Inc, shows the coordinate system of a multiple-layer forming fabric. The Z direction is perpendicular to the MD-CMD plane.

The multiple-layer forming fabric is currently the most popular in industry. The fabric is unique because filaments on either side of the sheet are distinct. To make the paper smooth, the filaments on the surface of the fabric in contact with the pulp are very fine (approximately 0.15mm in diameter, referred to as the "paper side"). To increase wear life and decrease running resistance, filaments in contact with the paper machine are made coarse (approximately 0.3mm diameter on the "machine side"), Johnson [6] and Johnson [7].

In addition to the coordinate system and number of layers in the forming fabric, what must also be defined is the woven structure in the fabric plane, i.e. MD-CMD plane. This structure is determined through the fabric shed value. The shed refers to the number of cross machine direction filaments in one fabric weave pattern. For a single layer of fabric, one number is needed. For multiple-layer fabrics, two numbers, one for the paper side and the other for the machine side, are required. The shed numbers for single, double and triple-layer fabrics are shown in Figure 1.6 [8].

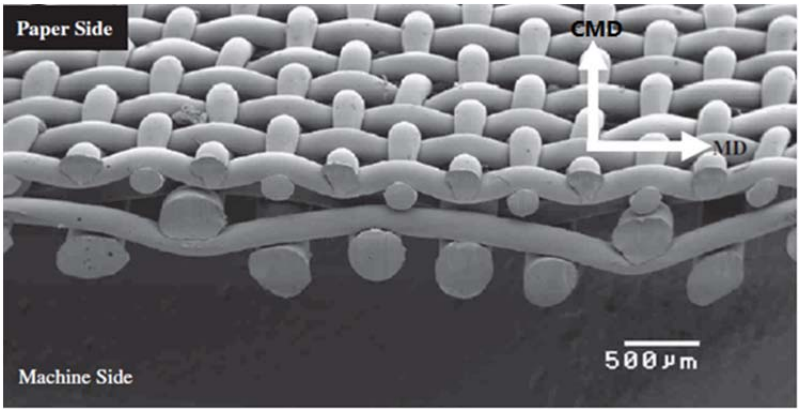


**Figure 1.5 A micrograph showing the two sides of a forming fabric**

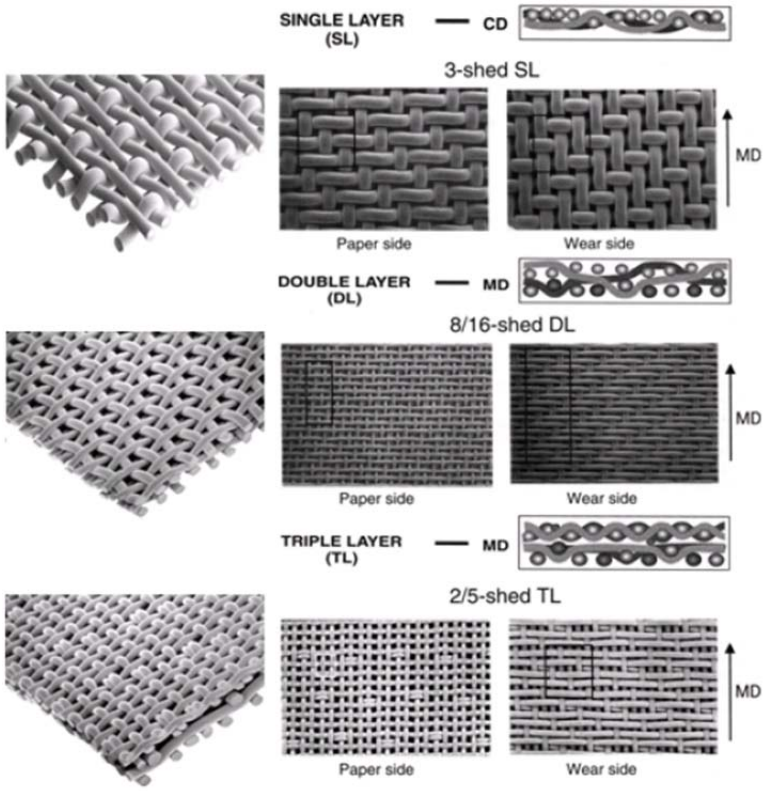


**Figure 1.6 Shed patterns for single, double and triple-layer fabric**

## 1.4 Wire Mark

A wire mark is the mark left on the paper web due to the formation wire, i.e. the forming fabric. Wire marks are undesirable as they can cause printing problems and substandard

optical results. There are two major types of wire marks: topographical wire marks and hydrodynamic wire marks. A topographical wire mark is the physical surface imprint of the forming fabric on the paper web [9]. A hydrodynamic wire mark is caused by unevenly distributed hydrodynamic forces of the flow through forming fabric, which results in the uneven fiber distribution in the paper web [10].

The focus of this thesis is on hydrodynamic wire marks, i.e. unevenly distributed fibers caused by hydrodynamic forces. Since the hydrodynamic forces placed on fibers are directly related to the velocity distribution of the flow around them, investigating the hydrodynamic wire mark involves an examination of the velocity distribution upstream from the forming fabric, where the paper web is formed. Therefore, the objective of this research is to measure the velocity distribution of the flow upstream from the forming fabric. With this data, we examine the non-uniformity of the velocity distribution and its possible effect on fiber distribution.

## 1.5 PIV Technique

We used Particle Image Velocimetry (PIV) to measure the detailed velocity distribution of the flow upstream from the forming fabric. The principle of PIV is discussed in this section. A detailed description of the setup will be shown in the second chapter.

Figure 1.7, courtesy to LAVISION, Inc, shows the general PIV setup. A double pulse laser head generates two laser beams over a time interval varying from nanoseconds to milliseconds. A cylindrical lens then transforms the laser beam into a laser sheet. When the laser sheet shines on the flow, the seeding particles in the flow are illuminated, and a

synchronized PIV camera captures a pair of images of the laser sheet plane with the illuminated seeding particles. A typical PIV image is shown in Figure 1.8.

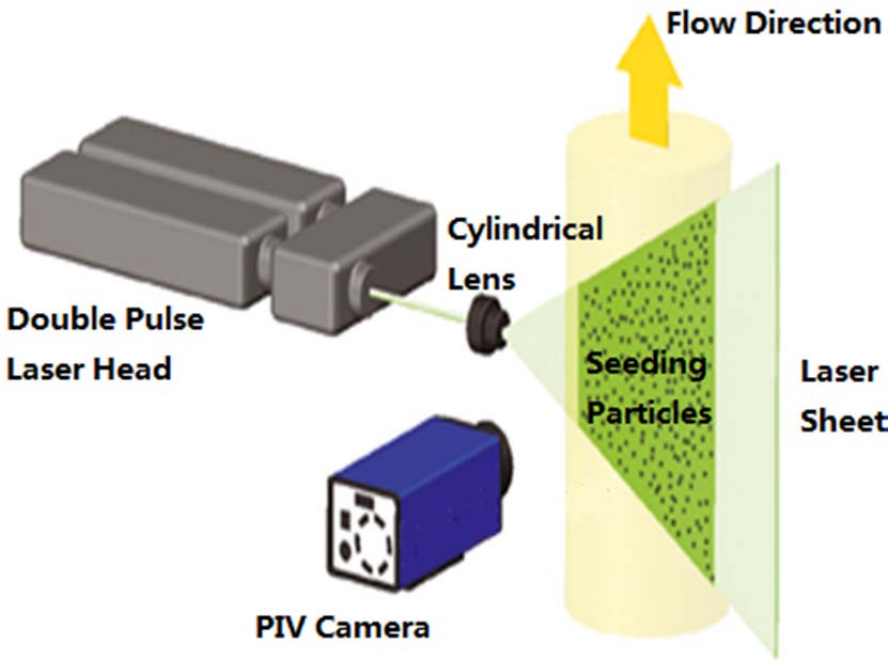


**Figure 1.7 Schematic figure of general PIV setup**

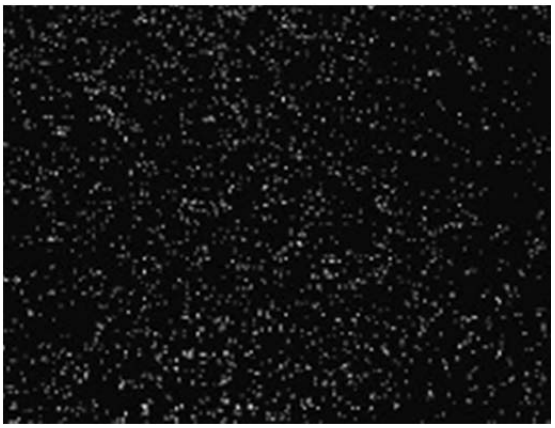

**Figure 1.8 Typical PIV image**

Figure 1.9, courtesy to TSI, Inc, shows the principles of PIV analysis. First, the images are divided into small windows called interrogation regions. Using a statistical method called cross-correlation, the displacement of each window from frame 1 to frame 2 is determined

from the peak point in the cross correlation function. The most probable displacement over the time interval is the average velocity vector in one interrogation window, i.e. $(\Delta\bar{x})/\Delta t \approx \bar{v}$, shown in Figure 1.10. By repeating these calculations, the velocity field of the entire image area is obtained.

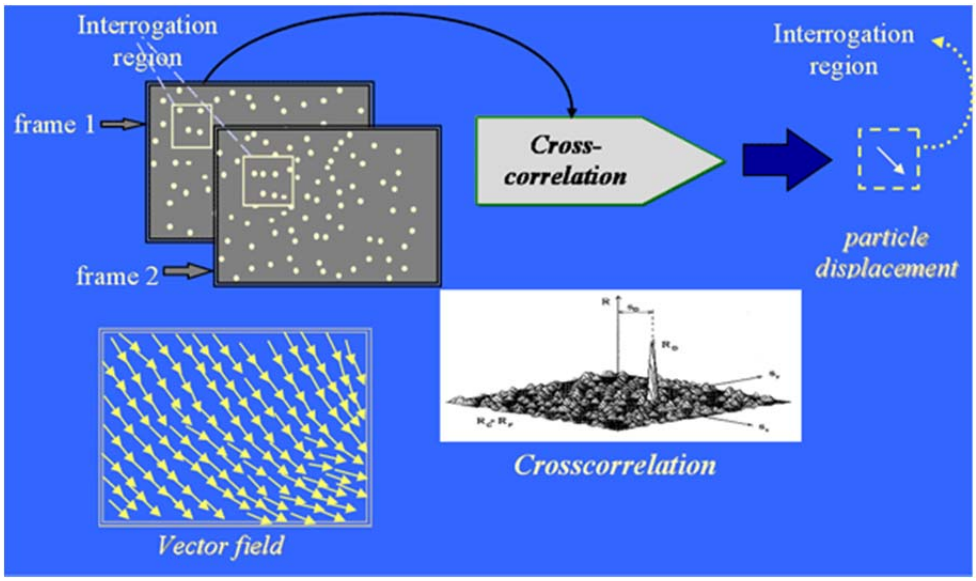


**Figure 1.9 PIV principle**

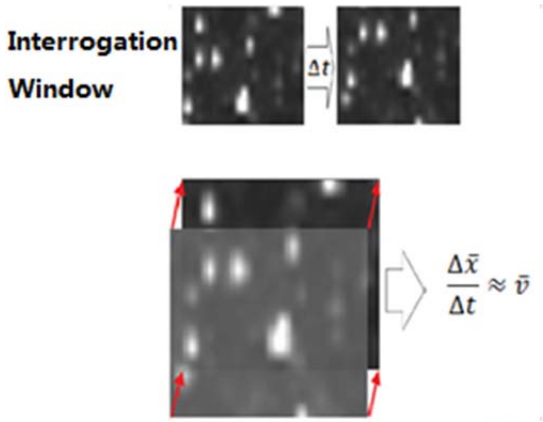


**Figure 1.10 Average velocity vector of one interrogation window obtained by cross correlation**

Details of the PIV technique, including the tracer particle size, light source, light sheet optics, digital image recording, post-process data analysis and mathematical background of the statistical PIV evaluation can be found in [11].

The previous five sections of this paper have given a detailed background of our research, including a review of the papermaking process, forming section, forming fabric, wire mark and PIV principle. The next section will provide a literature review of related work that has been conducted on forming fabrics.

## 1.6 Literature Review

This literature review is concerned with previous research on forming fabrics.

An investigation of the flow field through the forming section is critical, as any non-uniformity resulting from dewatering in the forming section cannot be changed in subsequent papermaking stages [1].

Forming fabric design has been improved in several ways in recent decades. Helle [12] found that the drainage rate is higher when fibers are oriented across the long knuckles of a single layer fabric. Beran [13] defined a significant parameter, the fiber support index (FSI), based on the average number of supports per fiber and the mean fiber length. He found that the FSI can determine the optimum fabric design for a particular paper machine, and that the higher the FSI, the finer the grade of the finished paper. Johnson [6] and Johnson [7] introduced another parameter, the drainage index (DI), which can be used to evaluate drainage performance. The higher the DI value, the better the drainage process. He also found that retention is better when using a shorter frame length. Moreover, he found that multiple-layer fabrics possess better fiber retention properties. Danby [14] investigated the impact of multilayer fabrics on sheet and wire mark formation, finding that coarse filaments on the machine side layer of the fabric increase multilayer fabric longevity. He also found that sheet quality is improved by using finer filaments on the paper side layer. Adanur [15] investigated

the effect that different forming fabrics had on sheet properties and formation. He found that higher DI and FSI levels produce stronger paper sheets. Helmer et al. [16] introduced another parameter formation index (FI) based on the Froude number, crowding number and aspect ratio of the flow depth to the fiber length. They found that higher FI and topside anisotropy levels result in higher late drainage rates. Xu et al. [17] found that an increase in center plane resistance caused by center layer structure in triple layer fabrics only retards the drainage at a lower basis weight.

Several articles have also been published on wire marks. Wire marks are non-uniform fiber distributions in the finished paper sheet which can develop while the forming fabric undergoes the drainage stage. As mentioned in Section 4, wire marks can be either topographical [9] or hydrodynamic [10]. The non-uniformity produced by wire marks has a profound effect on the printing quality of finished paper products, [2] and [3].

To investigate how the drainage of forming fabrics can produce wire marks, the non-uniformity of the flow field of the drainage process was investigated.

Research conducted by Dalpke et al. [18] shows that the Z-direction velocity of water passing through a forming fabric varies from 0.05 to 0.5 m/s depending on the impingement angle, fabric position and headbox jet velocity. This implies a Reynolds number between 6.5 and 65 based on the paper-side filament diameter. Therefore, most research concerned with the flow through forming fabrics has been based on the same Reynolds number, 6.5 to 65.

Due to the high complexity of the forming fabric three-dimensional structure, previous research on flow through forming fabrics considered simplification of fabric geometry. Huang [19] and Huang et al. [20] carried out a numerical investigation of flow through banks of cylinders at low Reynolds numbers (smaller than 150), finding that a downstream row of

cylinders has little influence on an upstream row of cylinders provided that the surface separation between the rows exceeds 0.7 times the upstream cylinder diameter ($Xs/d \geqslant 0.7$). Gilchrist et al. [21] measured the upstream velocity profile and pressure drop of the flow through two rows of cylinders. Their experimental findings were consistent with the simulations of Huang. Green et al. [22] conducted filament-level, three-dimensional simulations of the flow through single layer woven fabrics, finding that uneven filament spacing produces only localized changes in the flow field. Vakil et al. [23] found a novel method to produce accurate CAD models of real forming fabrics. These CAD models were then translated into CFD code to predict the filament-scale flow through a forming fabric. Flow non-uniformity and its probable effect on paper were considered in that article.

### 1.7 Thesis Objective, Approach and Hypothesis

According to the literature review, no experimental work has yet measured the detailed velocity distribution of flow through a woven forming fabric. This is the focus of this thesis.

The research work in this thesis is a continuation of the aforementioned studies on forming fabrics. First, using the PIV method, we measure the velocity field of the flow through forming fabrics. We then investigate the non-uniformity of the flow field, and the flow non-uniformity's possible effect on fiber distribution. We then compare PIV results with CFD simulations conducted on the same model used for the PIV measurements.

To execute the PIV measurements, an eighty times scale model of a real forming fabric, originally designed by AstenJohnson Inc., was manufactured by a Rapid Prototype Machine (Figure 1.11). Since the PIV experiments were conducted at the same Reynolds number present in real papermaking conditions, the results gleaned from these experiments should

reflect phenomena occurring in real papermaking processes. Because the pulp in front of the forming section possesses a very low concentration of fibers in water (0.7%), pure water was used in the experiments.

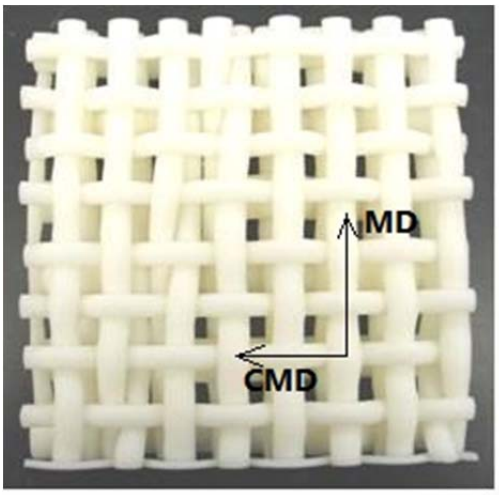


**Figure 1.11 Eighty times scale fabric model fabricated by a rapid prototype machine (31cm×31cm)**

The organization of this thesis is as follows: The 2nd chapter is a description of the experimental setup. The 3rd chapter presents the result for two dimensional velocity field of the flow through forming fabrics, which has already been published on TAPPI Papercon 2011. The 4th chapter includes the three dimensional velocity field measured by PIV; the flow non-uniformity's possible effect on fiber distribution; the CFD simulation results of the same flow condition and its comparison with PIV results. Finally, a brief set of conclusion and recommendations for future work are presented.

# Chapter 2: Experimental Methods

This chapter provides details of the experimental setup used for the PIV measurements. It includes the following three sections: flow loop setup, optical setup and configurations for best results.

## 2.1 Flow Loop Setup

Experiments were conducted in the University of British Columbia Pulp and Paper Center water/glycerin flow loop. The loop can create velocities of 1.5 to 8cm/s within a 31cm×31cm test section. We used a glycerin solutions with a dynamic viscosity 0.022 Pa·s, and an 80 times-scale fabric model, shown in Fig 1.11, to create different test-section Reynolds numbers between 10 and 65 based on different test-section velocities.

A schematic of the flow loop is shown in Figure 2.1. A Doerr 15HP, 1740RPM, 230/460V, 60Hz, 3-Phase motor is used to drive the device. A Toshiba Variable-Frequency Drive adjusts the motor speed and a Worthington 3FRB-101 acts as a pump. A 3" Rosemount flowtube is used as a flow meter. Diffuser, screen and honeycomb are used to straighten the flow. An image of the test-section with the scale forming fabric model installed is shown in Figure 2.2.

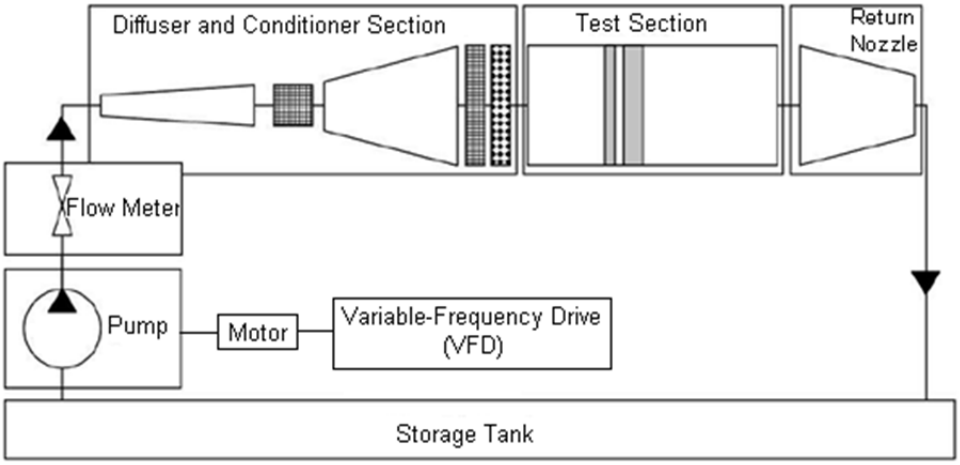


**Figure 2.1 UBC Pulp and Paper Center water/glycerin flow loop**

**Figure 2.2 31cm×31cm test section with forming fabric installed**

## 2.2 Optical Setup

A schematic of the PIV optical setup is shown in Figure 2.3. The flow was seeded with 20μm hollow glass beads. A cylindrical lens transforms a pulsed laser beam (generated by a New Wave GEMINI$^{TM}$ laser head) into a pulsed laser sheet. A synchronized PIV camera then captures pairs of images of the laser sheet plane with illuminated seeding particles. Using Dantec FlowManager software, we analyzed the images and obtained the velocity

distribution in the plane illuminated by laser sheet. Using a linear slide, the velocity distributions at different laser sheet planes (i.e. different MD and CMD planes) can be measured without adjusting the camera focus. This method is convenient for data collection and analysis since the dimensions of the field in view are always the same.

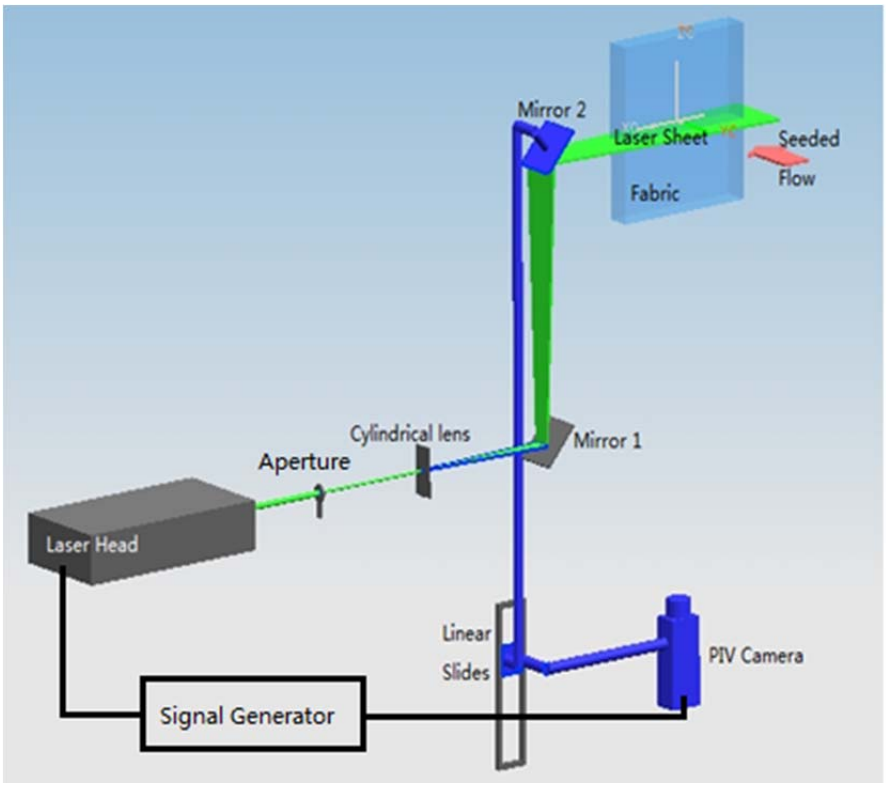


**Figure 2.3 Optical setup of the PIV experiment**

The details of the apparatus are as follows:

- Laser Head: New Wave Gemini PIV 15
- Aperture: Mounted Stainless Steel Iris, 12.0mm max
- Cylindrical Lens: f = 30.00mm, H = 20.00mm, L = 40.0mm, N-BK7 Plano-Convex Cylindrical Lens
- Mirror: 4”×6”
- Linear Slides: High-capacity Manual-position Slide, 9.56" Stroke
- PIV Camera: MEGAPLUS Model ES 1.0
- Signal Generator: Berkeley Nucleonics Corporation Model 500D

The signal generator is used to generate pulses that synchronize the laser head with the PIV camera. The time interval between two images is set depending on the maximum velocity of the PIV image area.

## 2.3 Configurations of Analysis Algorithm and Camera Lens

To analyze the data, pairs of images captured through the PIV measurement system were imported into Dantec Flowmanager software. Using this program, a cross correlation was conducted between each image pair to obtain the velocity distributions. To execute the cross correlation, the velocity in each interrogation window (ranging from 16pixels×16pixels to 64pixels×64pixels) was represented by an average velocity, which has been explained in section 1.5.

To determine which setup to use, we compared the velocity profiles of the same image pair by using different cross correlation window sizes, shown in Figure 2.4. We found that while larger window sizes produce smoother profiles, smaller window sizes come closer to matching the simulation results, which will be described in details in chapter 4. This occurs because larger window sizes can smooth out the peak velocity in the window, creating a smoother velocity profile. The smaller window size, however, reflects the real velocity distribution.

The resolution of the PIV camera is 1018 pixels by 1008 pixels. The field of view for the camera lens (75mm focal length) used for Figure 2.4 is 5.9d. So the size of 16pixels×16pixels window is approximately $\frac{16*5.9d}{1018} < \frac{d}{10}$, which is very small and the velocity variation in the interrogation window could be accurately represented by the average velocity vector of the window. So the velocity field obtained by using 16pixels×16pixels

interrogation window in cross correlation could precisely reflect the real velocity field. This conclusion is consistent with the result showed in Figure 2.4. Therefore, all of the cross correlation data presented in this thesis are derived from a 16pixels×16pixels interrogation window size.

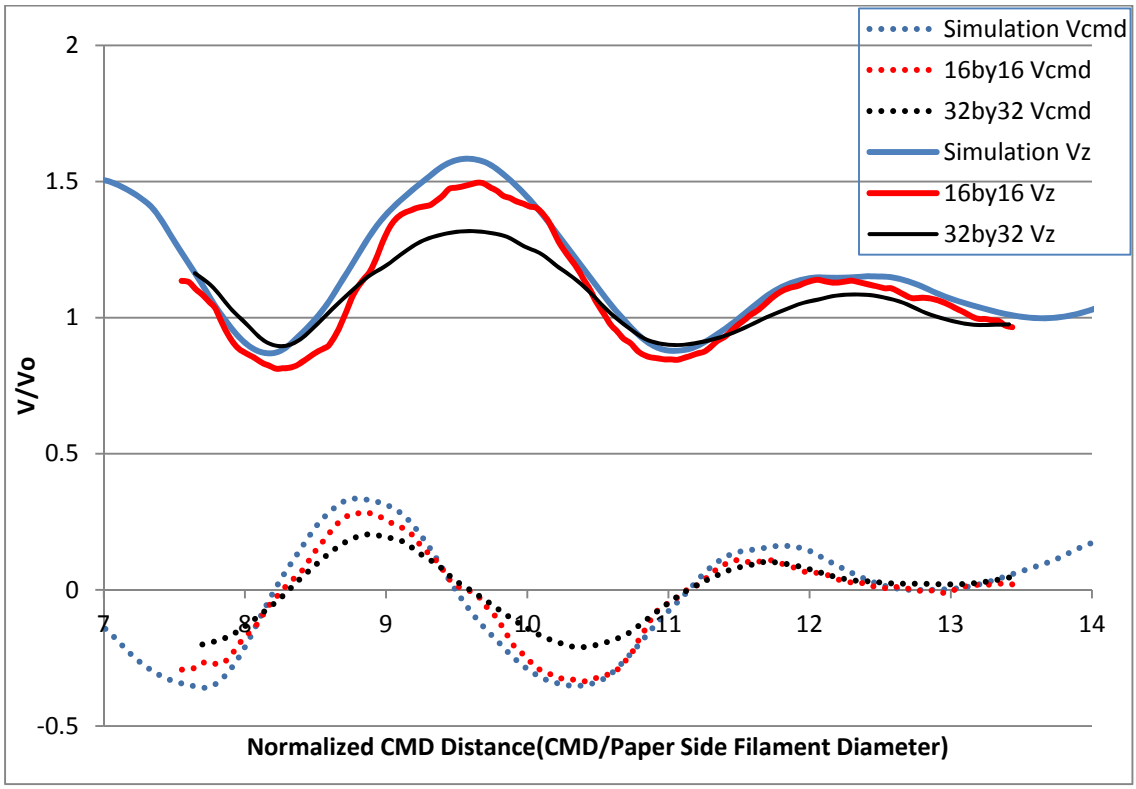


**Figure 2.4 Velocity profile comparison between different window sizes used for cross correlation analysis**

Another factor to discuss is the field of view of the PIV images. A larger field of view is desirable because it can capture more filaments in a single image. Keeping the focus distance constant, we can adjust the field of view by using a different camera lens with a different focal length. A longer focal length will produce a larger zoom ratio (image/object), and thus a smaller field of view. However, assuming that the analysis is based on a 16pixels×16pixels window size, a longer focal length camera will produce a smaller pixel size, resulting in a

smaller window size for cross-correlation. This will produce more accurate results. There is, hence, a tradeoff between the size of the field of view and the accuracy of results.

Figure 2.5 plots a velocity profile comparison between three different camera lenses: 28mm focal length lens, 75mm focal length lens and 150 mm focal length lens. It shows that the 28mm camera lens can produce a larger field of view at very low accuracy according to the simulation result; and the 75mm camera lens can produce a narrower field of view with higher accuracy. The results from the 150mm camera lens are very similar to the results obtained from the 75mm camera lens, meaning that the window size for the 75mm camera lens is small enough to produce an accurate result.

Because we are currently more concerned with the accuracy of the velocity measurements, we used a 75mm lens for all of the measurements presented in this thesis.

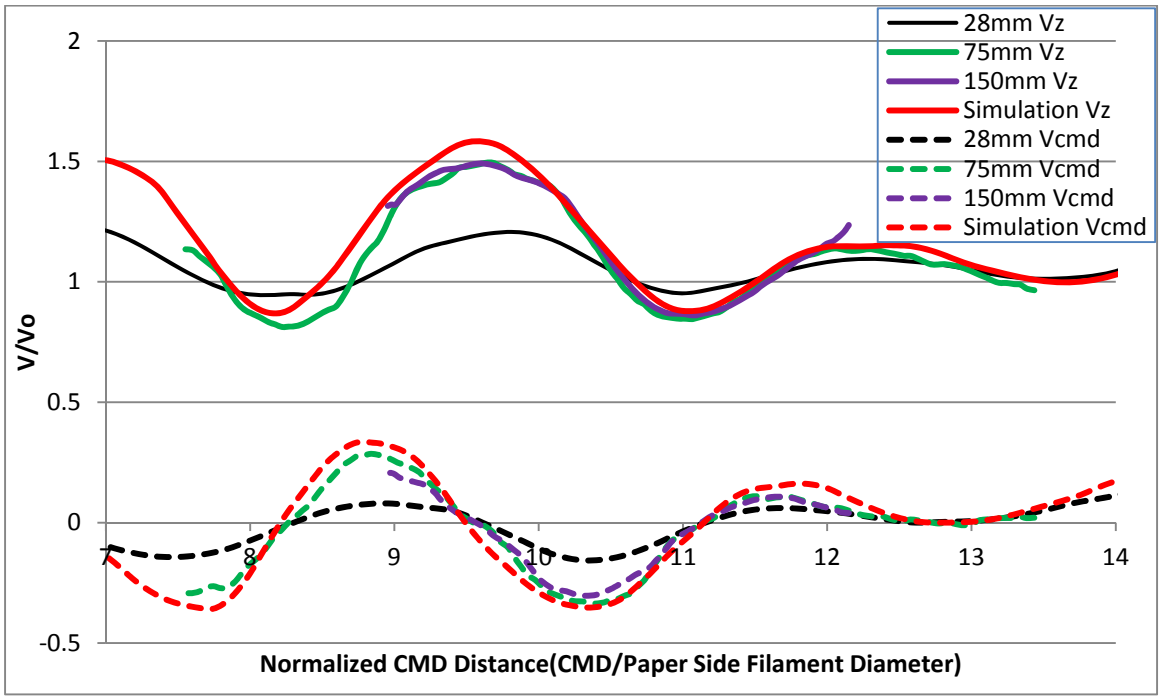


**Figure 2.5 Velocity profile comparison between different camera lenses with different focal lengths**

To summarize the experimental setup, we used 16pixels×16pixels as the window size for cross correlation analysis and a camera lens with a 75mm focal length to capture the PIV images. Other details on the apparatuses used in the optical and flow loop setups are also included in this chapter.

# Chapter 3: Two Dimensional PIV Results of Flow through Woven Fabrics[1]

## 3.1 Introduction

Papermaking involves three basic processes: forming, pressing and drying. During the forming stage, a dilute suspension of pulp and water, normally about 0.7% pulp by mass, is forced through a woven forming fabric, creating a pulp mat. Fibers are filtered from the suspension as water flows through the fabric, Adanur [1]. The fibrous mat is subsequently pressed and dried to create paper.

It is known that the flow non-uniformity upstream from the forming fabric can have a profound effect on the printed end product, Danby [2] and Danby et al. [3]. In order to create a high quality paper sheet of uniform density, it is important that the wet paper web possesses a highly uniform fiber mass distribution. Thus, a uniform velocity profile is desired on the upstream side of the fabric layer on which the mat is being formed.

The forming fabric structure is a complex, three-dimensional woven matrix consisting of machine direction (MD) and orthogonal cross machine direction (CMD) filaments in two or more layers. To enhance the paper's smoothness, the filaments on the fabric surface in contact with the pulp are very fine (approximately 0.15mm in diameter, referred to as the "paper side"). Filaments in contact with the papermachine are coarse (approximately 0.3mm diameter on the "machine side") to increase wear life and decrease running resistance, Johnson [6] and Johnson [7]. These characteristics are shown in Figure 1.5.

---

[1] A version of this chapter has been published. Peng, H., Green, S.I., 2011. PIV Measurements of Flow Immediately above Woven Fabrics. TAPPI PAPERCON 2011, 2149-2157.

To experimentally investigate flow through forming fabrics, a scale model of a real forming fabric, originally designed by AstenJohnson, was manufactured by a Rapid Prototype Machine (Figure 1.11). Because the pulp at the front of the forming section possesses a very low concentration of fibers in water (0.7%), pure water was used in the experiments.

Research conducted by Dalpke et al. [18] shows that the Z direction velocity of water through a forming fabric varies from 0.05 to 0.5 m/s depending on the impingement angle, position and headbox jet velocity. This implies a Reynolds number between 6.5 and 65 based on the paper-side filament diameter.

Due to the high complexity of the forming fabric three-dimensional structure, previous research on flow through forming fabrics has greatly simplified fabric geometry. Huang [19] and Huang et al. [20] carried out a numerical investigation of flow through banks of cylinders at low Reynolds numbers (smaller than 150), finding that a downstream row of cylinders has little influence on an upstream row of cylinders provided that the surface separation between the rows exceeds 0.7 times the upstream cylinder diameter ($Xs/d \geq 0.7$). Gilchrist et al. [21] measured the upstream velocity profile and pressure drop of the flow through two rows of cylinders. His experimental findings were consistent with the simulations of Huang. Green et al. [22] conducted filament-level, three-dimensional simulations of the flow through single layer woven fabrics, finding that uneven filament spacing produces only localized changes in the flow field. Vakil et al. [23] found a novel method to produce accurate CAD models of real forming fabrics. These CAD models were then translated into CFD code to predict the filament-scale flow through a forming fabric. Flow non-uniformity and its probable effect on paper were considered in the article.

The present work is a continuation of the aforementioned studies on forming fabrics. Here, we present the results of Particle Image Velocimetry (PIV) measurements of flow through woven fabrics. Following a description of our experimental methods, the article then discusses the PIV results and ends in a brief set of conclusions.

### 3.2 Experimental Methods

Experiments were conducted in the University of British Columbia Pulp and Paper Center water/glycerin flow loop. The loop can create velocities of 1.5 to 8 cm/s within its 31cm×31cm test-section. We used a glycerin solutions with a dynamic viscosity 0.022 Pa·s, and an 80 times-scale fabric model to create different test-section Reynolds numbers between 15 and 65 based on different test-section velocities.

A schematic of the flow loop is shown in Figure 2.1. An image of the test-section with the forming fabric installed is shown in Figure 2.2. The schematic of the PIV optical setup is shown in Figure 2.3. The flow was seeded with 20μm hollow glass beads. A cylindrical lens transformed a pulsed laser beam (generated by a New Wave GEMINI$^{TM}$ laser head) into a pulsed laser sheet. The synchronized PIV camera then captured pairs of images of the laser sheet plane with illuminated seeding particles. Using Dantec FlowManager$^{TM}$ software, we analyzed the images and obtained the velocity distribution of the plane illuminated by laser sheet. Using a linear slide, the velocity distribution at different laser sheet planes (i.e. different MD planes) could be measured without adjusting the camera focus. This is convenient for data collection and analysis since the dimensions of the field in view are always the same.

### 3.3 Two Dimensional PIV Results and Discussion

PIV measurements were conducted for different MD planes, shown in Figure 3.1, at different Reynolds numbers. In order to keep the plots uncluttered only Figure 3.2 has uncertainty bars, which represent the 95% confidence interval based on 30 PIV image pairs for each configuration. The origin, located at the bottom right corner of the fabric model, and direction of the coordinate system is shown in Figure 3.1. The MD and CMD distances are normalized by the paper side filament diameter of the fabric model and the normalized length in MD and CMD are both about 20. The scale model used in the flow loop is smaller than one fabric repeat. To avoid contamination of the results by wall boundary layer effects, only the portion of the fabric away from the test section walls was studied.

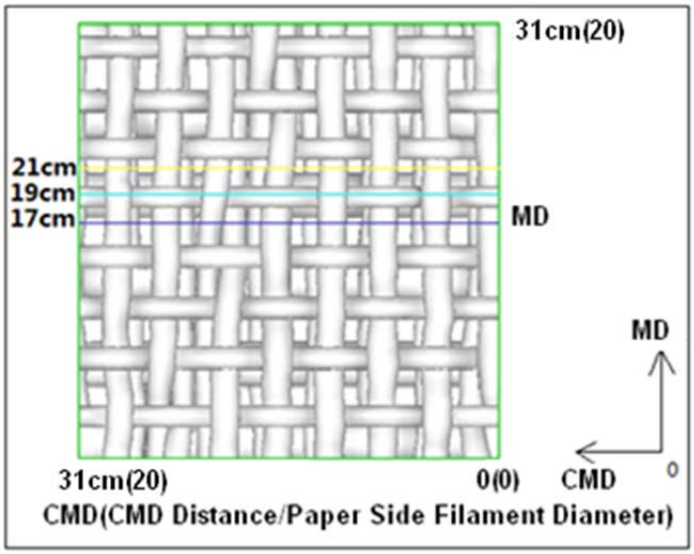


**Figure 3.1 MD-CMD view of the scale fabric model**

Figure 3.2 shows that the RMS variation of CMD velocities is about 15.6% of the average Z direction velocity in the CMD line on the plane MD=17cm (Normalized MD=11), and 0.25d (d=paper side filament diameter) above the fabric top surface. The highest and average relative uncertainties for the ZD velocity in the CMD line are ±7.0% and ±2.5%, respectively, of the far field velocity ($V_0$). The highest and average relative uncertainties for the CMD

velocity in the CMD line are ±2.8% and ±1.7%, respectively, of the far field velocity ($V_0$). The horizontal uncertainty is ±0.5mm because the minimum scale of calibration is 1mm.

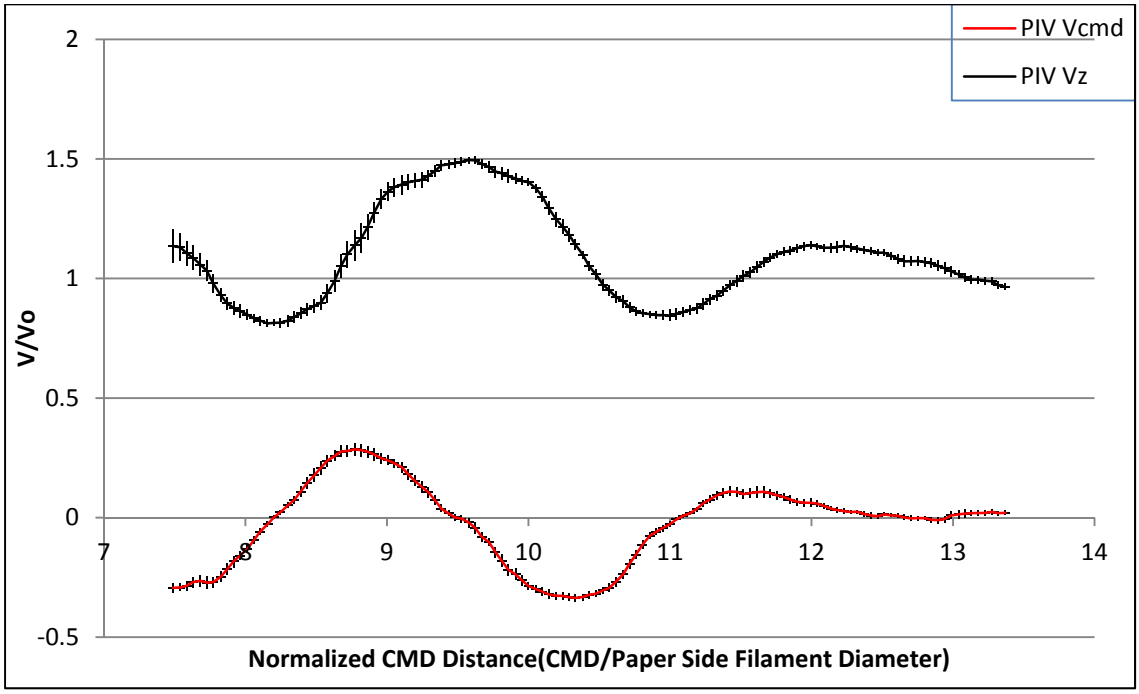


**Figure 3.2 Velocity vs. CMD Distance, at MD=17cm (11), 0.25d upstream of the fabric model; Re=35**

Figure 3.3 shows that the deviation of the normalized Z direction velocity decreases from 19.9% at a plane 0.25d upstream the forming fabric to 2.9% at a plane 1.5d upstream. It also shows that the deviation of the normalized CMD velocity decreases from 16.9% at a plane 0.25d upstream the forming fabric to 1.9% at a plane 1.5d upstream. This means that the flow non-uniformity caused by the forming fabric is only significant within about 1.5 paper-side-filament-diameters upstream from the forming fabric.

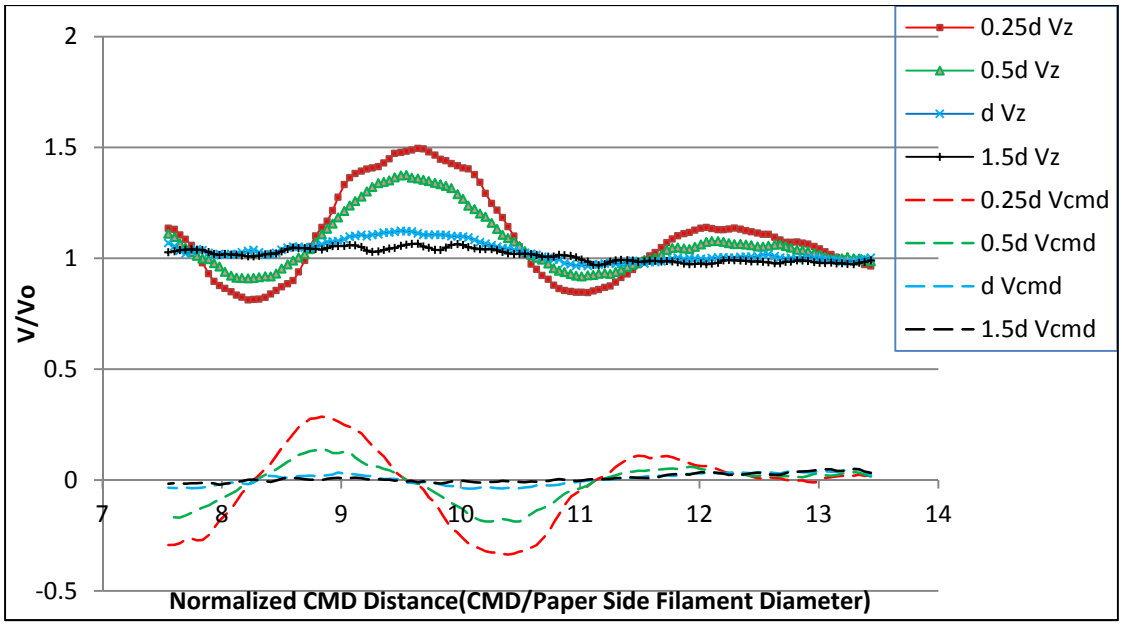


**Figure 3.3 Velocity comparison of different distances upstream from the fabric model; MD=17cm, Re=35**

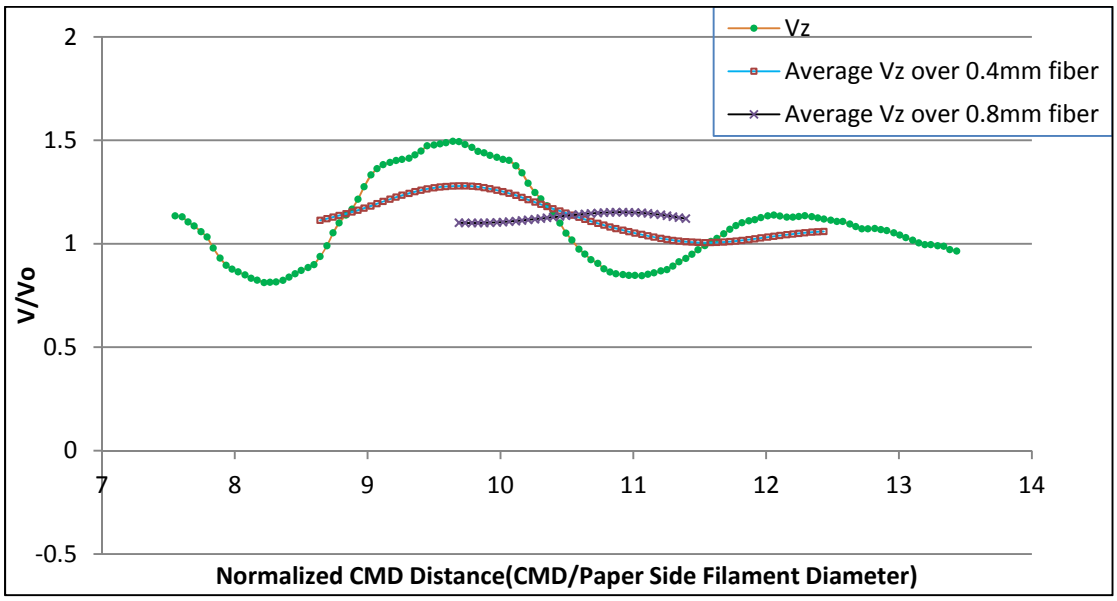


**Figure 3.4 Comparison of average ZD velocity over different fiber length, 0.25d upstream, MD=17cm, Re=35**

Since pulp fibers have a length scale broader than the spaces between forming fabric filaments, the fibers are exposed to flow field forcing related to the average velocity along

the fiber length. Here we assume that a 0.8mm (length) fiber is oriented parallel to the CMD, and we average over a CMD line with length equal to the fiber length. With this averaging (Figure 3.4), the normalized velocity deviation is reduced from 19.9% to 1.9%. For the majority of wood fibers, most of which are longer than 0.8mm, the averaging effect would be even greater. We can therefore predict that as long as the fibers are uniformly distributed in the approach flow, they will remain so while interacting with this forming fabric.

Figure 3.5 shows the velocity profile at three different Reynolds numbers. The normalized Z direction velocity profile varies less than 8% when Reynolds number increases from 15 to 65 since all three Z direction velocity profiles fall within the 8% error bars as shown in the figure. Considering the uncertainty for PIV measurements, the difference between these different Reynolds numbers could not be distinguished.

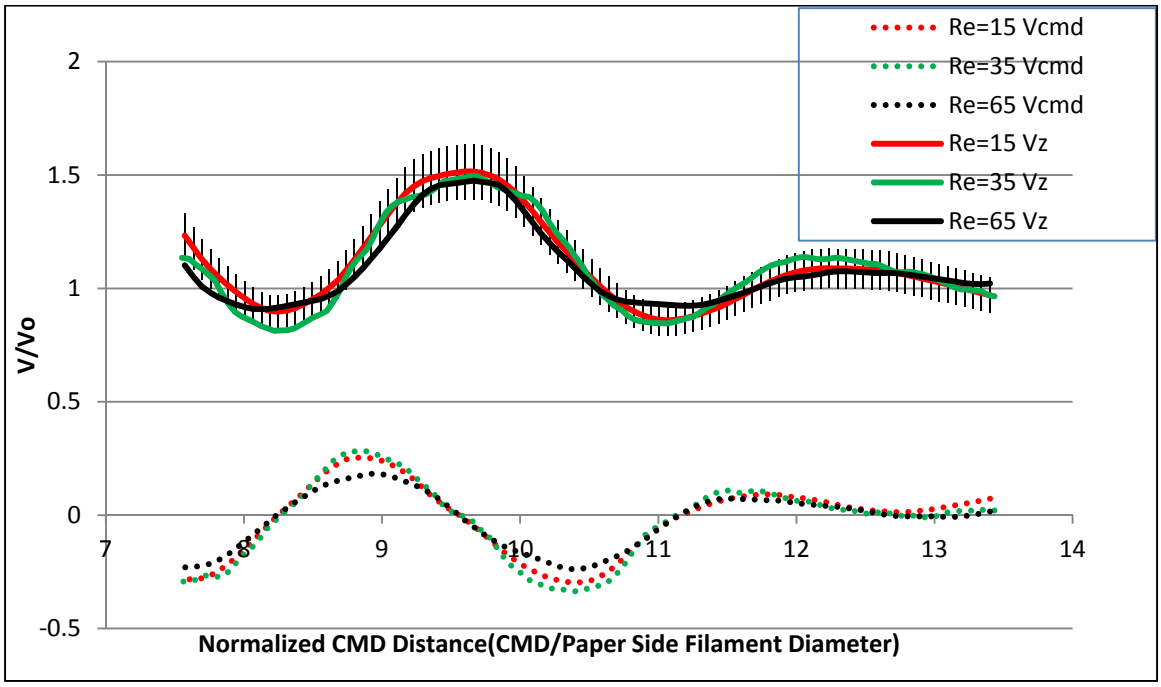


**Figure 3.5 Velocity profile comparison between different Reynolds numbers, 0.25d upstream, MD=17cm**

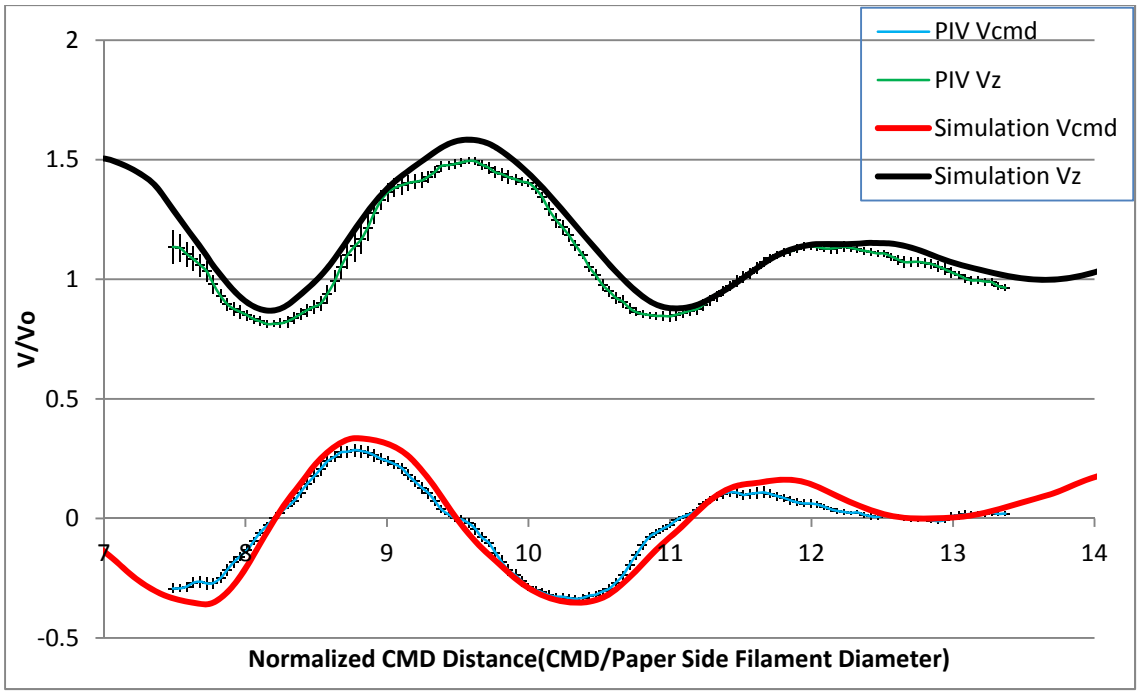


**Figure 3.6 Velocity comparison between Simulation and PIV measurements, 0.25d upstream, MD=17cm, Re=35**

Using FLUENT™ and following methods described by Green et al. [22], we conducted CFD simulations of flow through the same fabric model. As shown in Figure 3.6, the simulation results are very similar to the PIV measurements and never differ by more than 7%. Simulations conducted at higher and lower Reynolds numbers were also in fairly good agreement with the experimental measurements.

## 3.4 Conclusions

PIV measurements of flow through a woven fabric at the Reynolds numbers typical of papermaking have been performed. Our studies show that the RMS variation of CMD velocities is about 15.6% of the average ZD velocity at a distance of 0.25d above the fabric. The deviation of the normalized ZD velocity decreases from 19.9% at a plane 0.25d upstream

the forming fabric to 2.9% at a plane 1.5d upstream. The deviation of the normalized CMD velocity decreases from 16.9% at a plane 0.25d upstream the forming fabric to 1.9% at a plane 1.5d upstream. This means that the flow non-uniformity caused by the fabric weave is constrained to a short distance above the fabric. This non-uniformity is, however, not particularly felt by fibers, which possess length scales that average the local velocity field. Due to the uncertainty of PIV measurement, the difference between different Reynolds numbers from 15 to 65 could not be distinguished. CFD simulations of the same flow were consistent with the PIV measurements within $\pm$ 7%.

# Chapter 4: Three Dimensional PIV Results of Flow through Woven Fabrics

## 4.1 Introduction

At the forming stage of the papermaking process, a very dilute pulp suspension is spread over a woven forming fabric to create a pulp mat. Fibers are filtered from the suspension as the water flows through the fabric, Adanur [1]. The fibrous pulp mat is then pressed and dried to produce paper.

One important property of high quality paper is a uniform density distribution. It is known that the flow non-uniformity caused by woven fabrics can unevenly distribute fibers in the wet pulp web. This creates an uneven density distribution in the wet web, which has a profound effect on the printed end products, Danby [2] and Danby et al. [3]. To produce high quality paper, a uniform velocity distribution upstream from the forming fabric is desirable.

The forming fabric structure is a complex three-dimensional woven matrix, consisting of machine direction (MD) and orthogonal cross machine direction (CMD) filaments in two or more layers. To create smooth paper, the filaments on the surface of the fabric in contact with the pulp are very fine (approximately 0.15mm in diameter, referred to as the "paper side"). To increase wear life and decrease running resistance, coarse filaments (approximately 0.3mm diameter on the "machine side") in contact with the paper machine are used, Johnson [6] and Johnson[7]. These characteristics are shown in Figure 1.5.

To experimentally investigate flow through forming fabrics, a scale model of a real forming fabric, originally designed by AstenJohnson, was manufactured by a Rapid Prototype

Machine (Figure 1.11). Since the pulp at the front of the forming section possesses a very low concentration of fibers in water (0.7%), pure water was used in the experiments.

Research conducted by Dalpke et al. [18] shows that the Z direction (ZD) velocity of water moving through a forming fabric varies from 0.05 to 0.5 m/s depending on the impingement angle, position and headbox jet velocity. This implies a Reynolds number between 6.5 and 65 based on the paper-side filament diameter. Our experiment also runs on a Reynolds number within this range. Most of the results presented in this article were produced at a Reynolds number of 35.

Due to the high complexity of the forming fabric three dimensional structure, previous research on flow through forming fabrics has greatly simplified fabric geometry. Huang [19] and Huang et al. [20] carried out a numerical investigation of flow through banks of cylinders at low Reynolds numbers (smaller than 150). They found that a downstream row of cylinders had little influence on an upstream row of cylinders, provided that the surface separation between the rows exceeded 0.7 times the upstream cylinder diameter ($Xs/d \geq 0.7$). Gilchrist et al. [21] measured the upstream velocity profile and pressure drop of the flow through two rows of cylinders. Their experimental findings were consistent with the simulations of Huang. Green et al. [22] conducted filament-level three-dimensional simulations of the flow through single-layer woven fabric, finding that uneven filament spacing produces only highly localized changes in the flow field. Vakil et al. [23] found a novel method to produce accurate CAD models of real forming fabrics. These CAD models were then input into CFD code to predict the filament-scale flow through a forming fabric. It also discussed the flow non-uniformity and its probable effect on paper. In chapter 3 of this thesis, the experimental

results of the velocity distribution on one CMD line of the flow through forming fabrics were presented.

The work in this chapter is a continuation of the aforementioned studies on forming fabrics. Here, we present completed PIV measurement results (velocity distribution on a whole MD-CMD plane) of the flow through woven fabrics. Following a description of our experimental methods, the article discusses the PIV results, the simulation results and ends in a brief set of conclusions.

## 4.2 Experimental Methods

Experiments were conducted in the University of British Columbia Pulp and Paper Center water/glycerin flow loop. The loop can create velocities of 1.5 to 8 cm/s within its 31cm×31cm test-section. We used a glycerin solutions with a dynamic viscosity 0.022 Pa·s, and an 80 times-scale fabric model to create different test-section Reynolds numbers between 10 and 65 based on different test-section velocities.

A schematic of the flow loop is shown in Figure 2.1. An image of the test-section with the forming fabric installed is shown in Figure 2.2. The schematic of the PIV optical setup is shown in Figure 2.3. The flow was seeded with 20μm hollow glass beads. A cylindrical lens transformed a pulsed laser beam (generated by a New Wave GEMINI$^{TM}$ laser head) into a pulsed laser sheet. The synchronized PIV camera then captured pairs of images of the laser sheet plane with illuminated seeding particles. Using Dantec FlowManager$^{TM}$ software, we analyzed the images and obtained the velocity distribution of the plane illuminated by laser sheet. Using a linear slide, the velocity distribution at different laser sheet planes (i.e. different MD planes) could be measured without adjusting the camera focus. This method is

convenient for data collection and analysis since the dimensions of the field in view are always the same. The fabric model was then rotated by 90º to measure the MD velocity at different CMD planes.

### 4.3 Three Dimensional PIV Results and Discussion

PIV measurements were conducted of multiple MD and CMD planes at different Reynolds numbers, shown in Figure 4.1. In order to keep the plots uncluttered, uncertainty bars are shown only in Fig4.2 and Figure 4.11. Uncertainty bars represent a 95% confidence interval based on 30 PIV image pairs for each configuration. The origin, located at the bottom right corner of the fabric model, and direction of the coordinate system is shown in Figure 4.1. The MD and CMD distances are normalized by the paper side filament diameter, labeled as d, of the fabric model and the normalized length in MD and CMD are both about 20. The scale model used in the flow loop is smaller than one fabric repeat. To prevent wall boundary layer effects from contaminating the results, we limited our study to the portion of the fabric located at a distance from the test section walls.

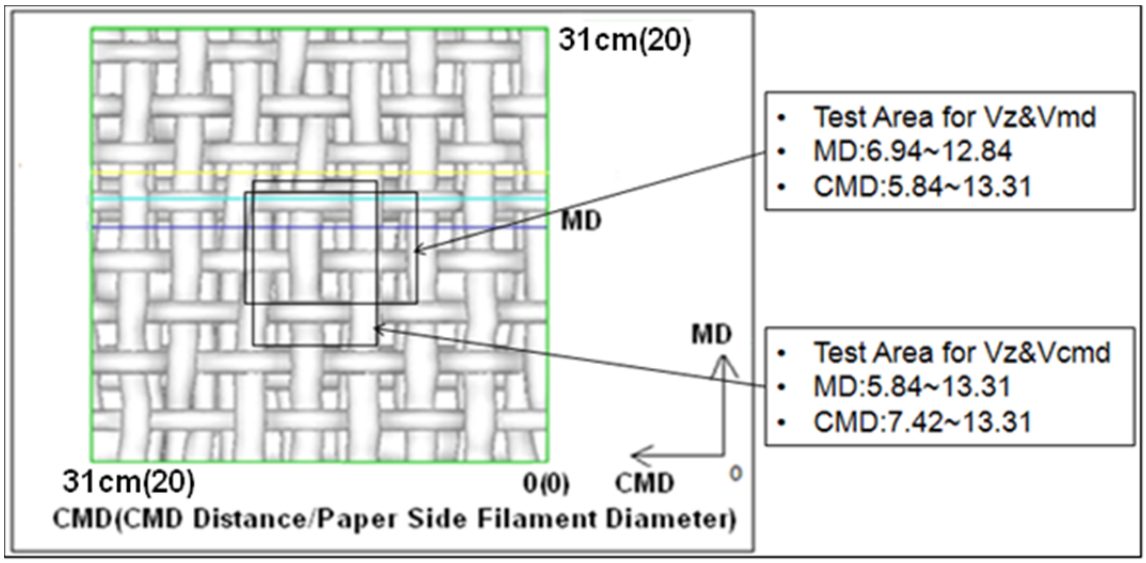


**Figure 4.1 MD-CMD view of the scale fabric model with test area**

The results will be presented in three sections. The first section presents the results for Vz and Vcmd based on PIV measurements conducted using the CMD velocity setup (i.e. illumination plane was normal to MD). The second section presents results for Vz and Vmd by using the MD velocity setup, i.e. illumination plane was normal to CMD. This was achieved by rotating the fabric model by 90º about the ZD. The third section compares the ZD velocities obtained by the two orthogonal PIV setups.

### 4.3.1 Vz and Vcmd Results

Figure 4.2 shows typical ZD and CMD velocity distributions along a typical CMD line. The highest and average relative uncertainties for ZD velocity in the CMD line are ±7.0% and ±2.5% respectively. The highest and average relative uncertainties for CMD velocity along the same CMD line are ±2.8% and ±1.7% respectively. As mentioned above, these uncertainties are calculated based on 30 measurements, with a 95% confidence interval. The horizontal uncertainty is ±0.5mm because the minimum scale of calibration is 1mm. In order to produce an uncluttered plot the uncertainty bars are only plotted in Figure 4.2 and 4.11.

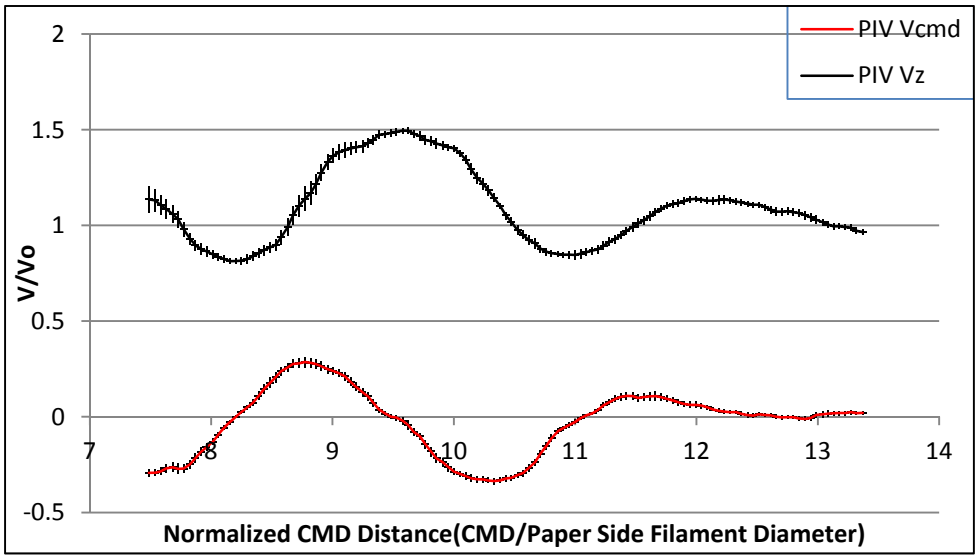


**Figure 4.2 Velocity vs. CMD distance, MD=17cm (11), 0.25d upstream, Re=35**

Figure 4.3 and Figure 4.4 respectively show the ZD and CMD velocity contours at the plane 0.25d above the forming fabric. In this plane, the standard deviation of the ZD velocity and CMD velocity are 19.7% and 15.3%, respectively, when normalized by far field velocity Vo.

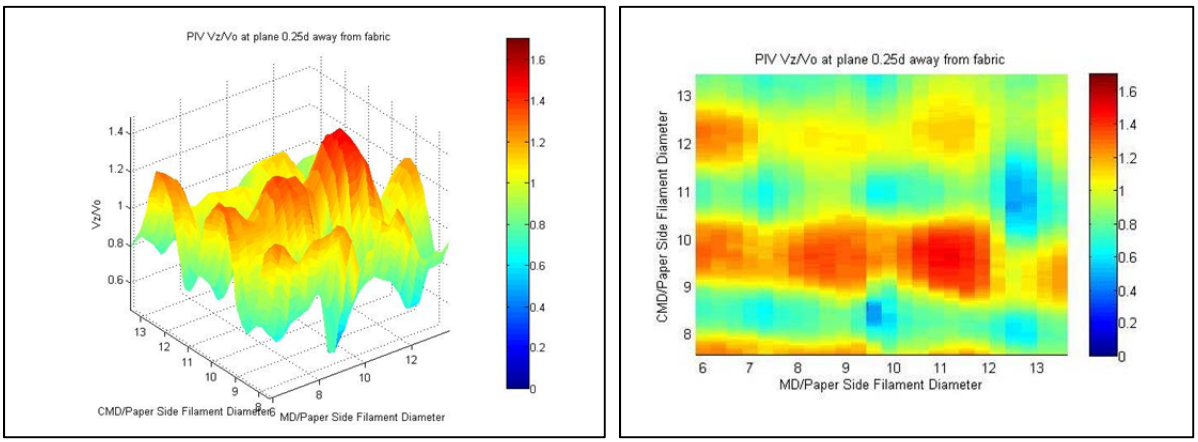


(a) Isometric view (b) Top view

**Figure 4.3 ZD velocity contours in CMD velocity setup**

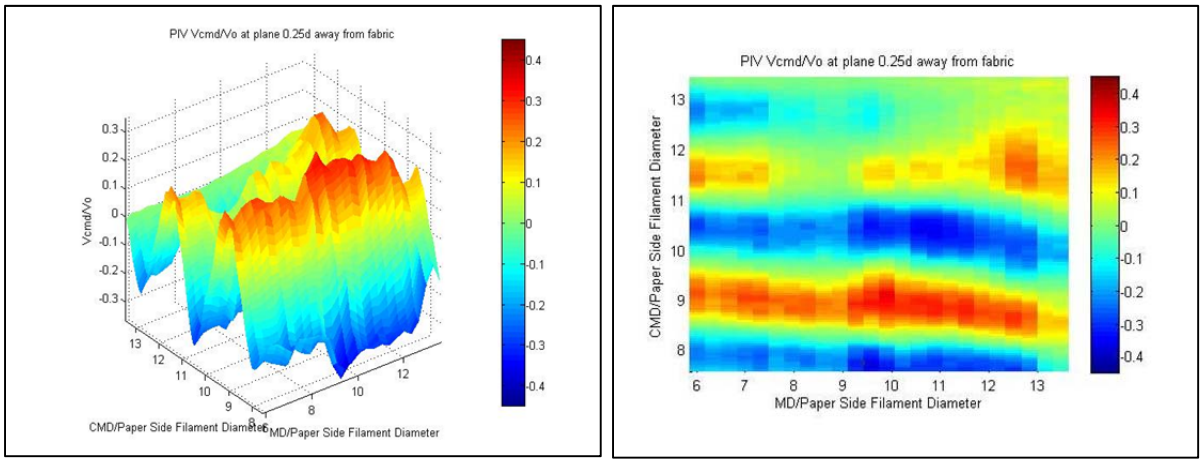


(a) Isometric view (b) Top view

**Figure 4.4 CMD velocity contours in CMD velocity setup**

Figure 4.5 shows that the normalized ZD and CMD velocity deviations decrease from 19.7% to 4.2% and 15.3% to 1.9%, respectively, when the distance to the paper side surface of the

forming fabric increases from 0.25d to 1.5d. Figure 4.6 shows that the highest Z direction velocity is about 3.3 times of the lowest Z direction velocity at a plane 0.25d above the fabric. This value diminishes to 1.2 when the plane elevation increases to 1.5d. Figure 4.7 compares the ZD velocity contour between planes at a distance 0.25d and 1.5d above the fabric. The figure clearly shows that the velocity contour is nearly uniform at the 1.5d plane. According to Figure 4.8, it is the same case for the CMD velocity. The results from Figure 4.5 to Figure 4.8 demonstrate that the non-uniformity caused by the fabric is only significant within a limited range, i.e. 1.5d above the fabric top surface.

Due to the uncertainty of PIV measurements, which will be discussed in section 4.3.4, the deviation in Figure 4.5 will always be larger than zero, even at a distance further away from the fabric. For the same reason, the maximum/minimum ZD velocity in Figure 4.6 will always be larger than one. The contours in Figure 4.7 and Figure 4.8, on the other hand, will never achieve perfect uniformity. The near constancy of the velocity standard deviation for 1.5d and 2d plane indicates that the remaining non-uniformity at the 1.5d plane is mainly caused by experimental error rather than the forming fabric's woven structure.

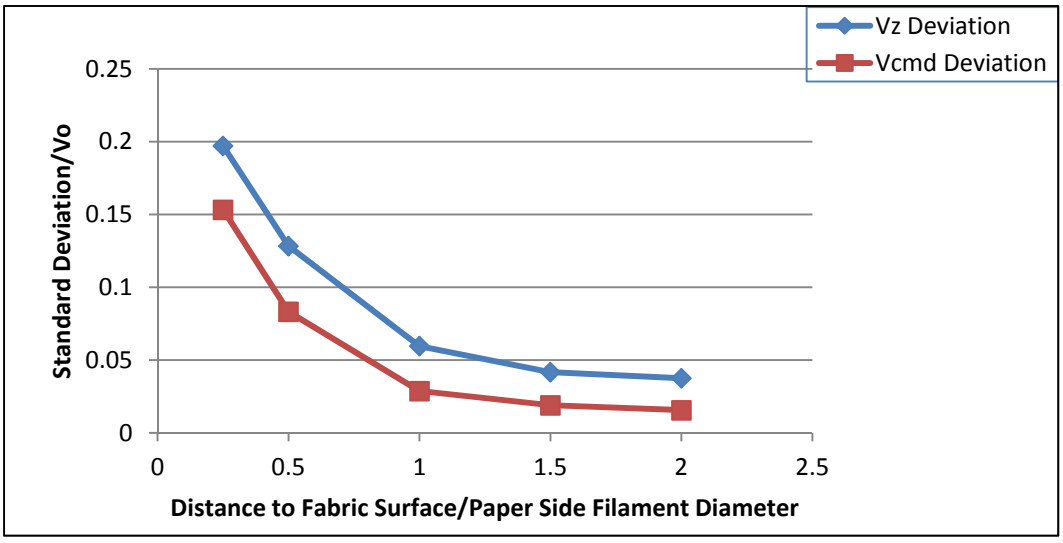


**Figure 4.5 Velocity standard deviation vs. Distance to fabric surface, Re=35, CMD velocity setup**

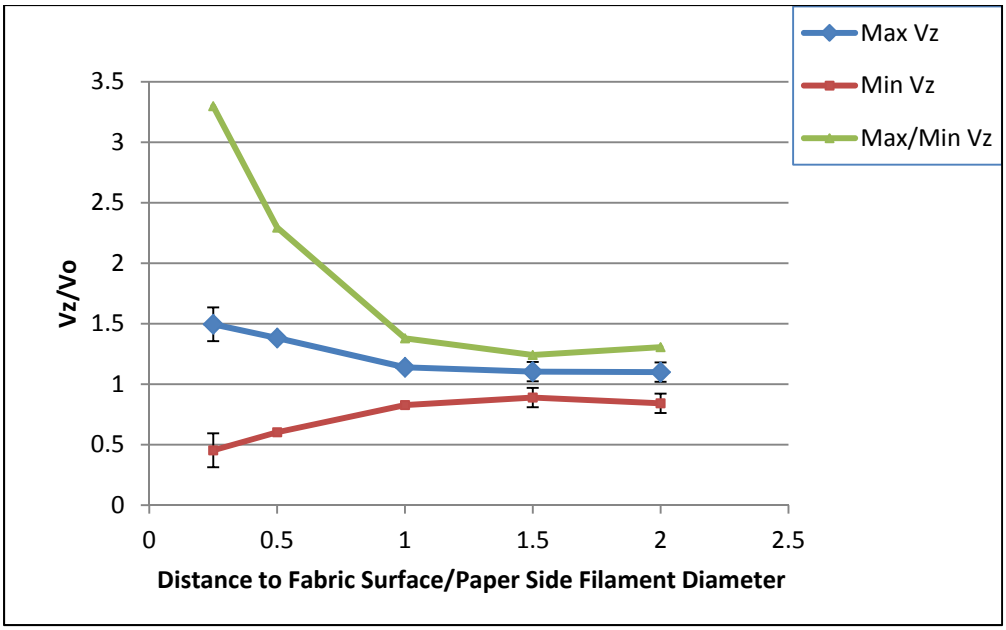


**Figure 4.6 Highest and lowest ZD velocity vs. Distance to fabric surface, Re=35, CMD velocity setup**

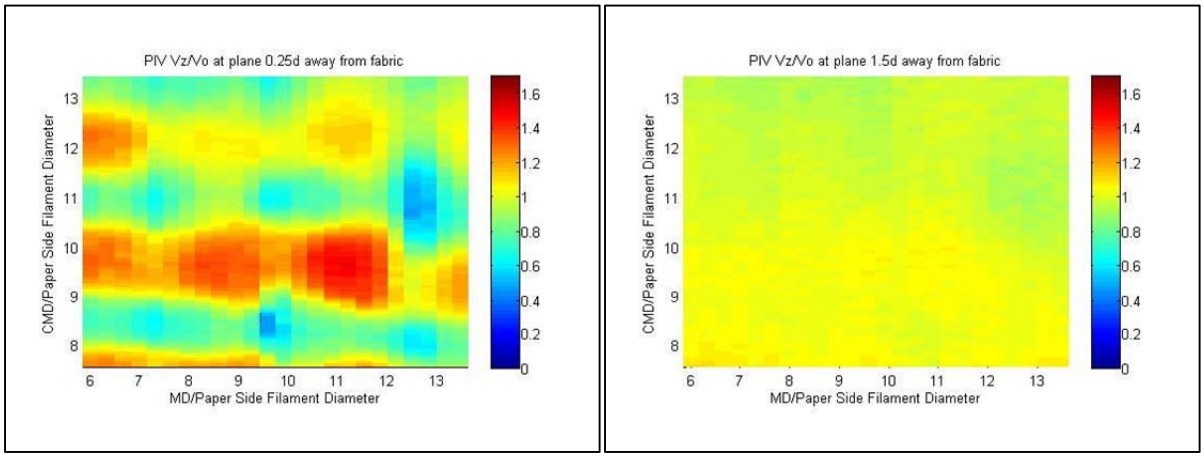


(a) 0.25d upstream (b) 1.5d upstream

**Figure 4.7 ZD velocity contour at different distances from the fabric surface, CMD velocity setup**

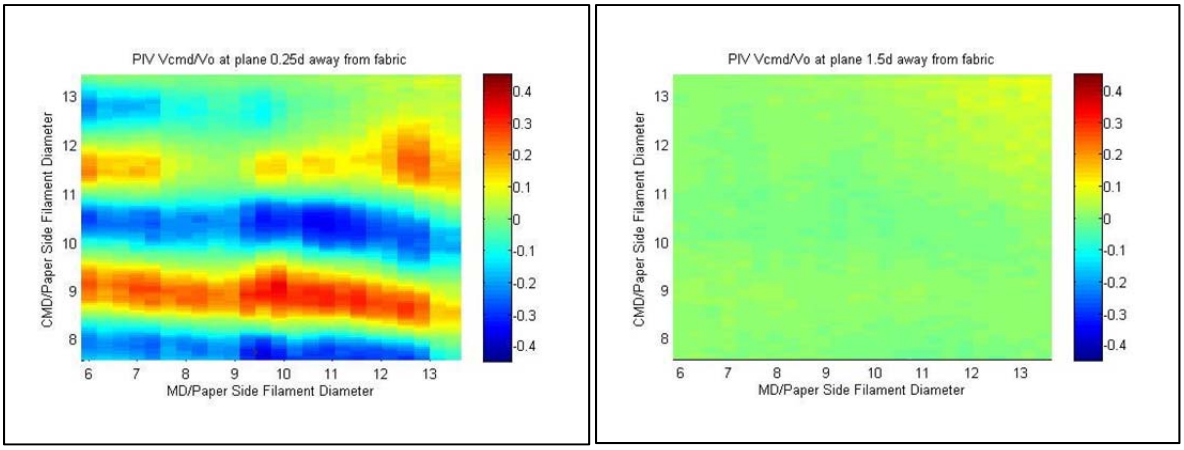


(a) 0.25d upstream (b) 1.5d upstream

**Figure 4.8 CMD velocity contour at different distances from the fabric surface, CMD velocity setup**

Since pulp fibers have a length scale that is longer than the forming fabric filament spacing, they are exposed to flow field forcing that is related to the average velocity along the fiber length. Here we assume that a fiber is oriented in CMD, and we average over a CMD line with a length equal to the fiber length. With this averaging (Figure 4.9), the velocity non-uniformity in CMD is smoothed out when the fiber length equals 0.8mm. Since many wood fibers are longer than 0.8mm, and an increase in fiber interaction raises the fiber length scale, the averaging effect would be even greater in the real papermaking process. Although CMD filaments in the fabric still cause non-uniformity in MD, this non-uniformity will be reduced if the fiber is oriented in MD, shown in Figure 4.18. Since the fibers are randomly oriented in the approach flow, the real average velocity contour will be more uniform than the contours shown in Figure 4.9. This is especially true in MD. Figure 4.10 shows that the ratio between the maximum and minimum average ZD velocity over a CMD oriented fiber will reduce from 3.3 to 1.6 when the fiber length increases to 0.8mm. For the aforementioned reason, this reduced value will come even closer to 1 for longer, randomly oriented fibers. As a result, the

non-uniformity is smoothed out. Given the results presented in Figure 4.9 and Figure 4.10, we can conclude that fibers that are uniformly distributed in the approach flow will remain so while interacting with this forming fabric.

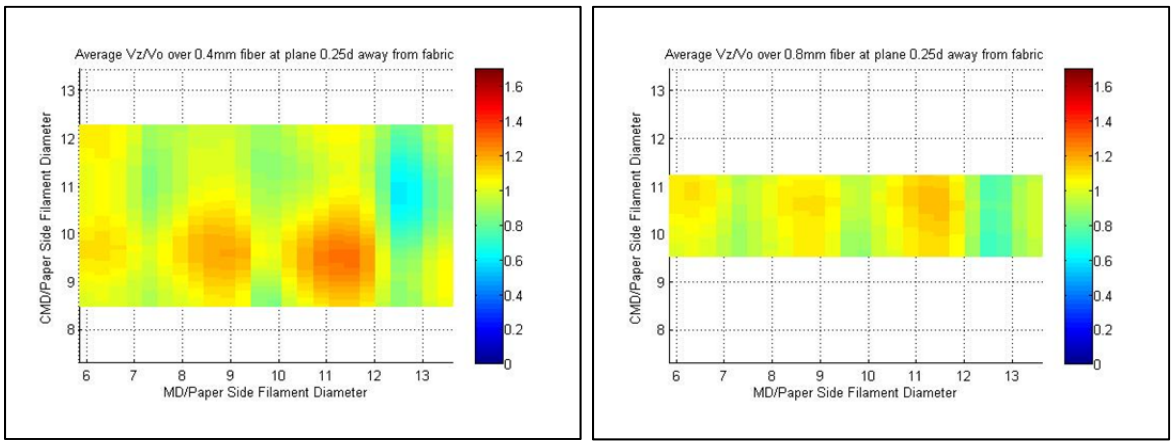


(a) 0.4mm fiber (b) 0.8mm fiber

**Figure 4.9 Contour of average ZD velocity over a CMD fiber, 0.25d upstream, Re=35**

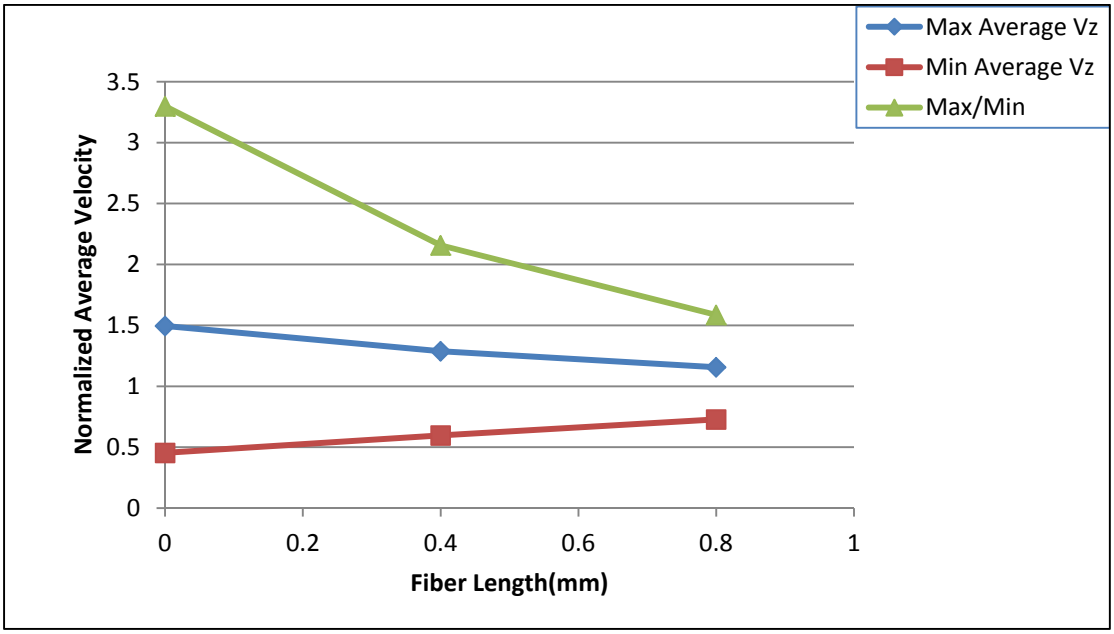


**Figure 4.10 Average ZD velocity over a CMD fiber, 0.25d upstream, Re=35**

### 4.3.2 Vz and Vmd Results

In order to measure the MD velocity, PIV images must be taken in a plane parallel to MD. We achieved this by rotating the fabric model 90º in ZD. With this step no further adjustments were required for other optical setups. Using this setup the ZD velocity was measured again with MD velocity. Here we present the results of our tests for ZD velocity and MD velocity. We then compare the results of ZD velocity produced by the two different setups.

Figure 4.11 shows that the highest and average relative uncertainties for ZD velocity in the MD line are ±5.1% and ±3.3% respectively. The highest and average relative uncertainties for MD velocity in the MD line are ±3.3% and ±1.5% respectively. As mentioned above, these uncertainties are calculated using 30 measurements, at a 95% confidence interval. The horizontal uncertainty is ±0.5mm because the minimum scale of calibration is 1mm.

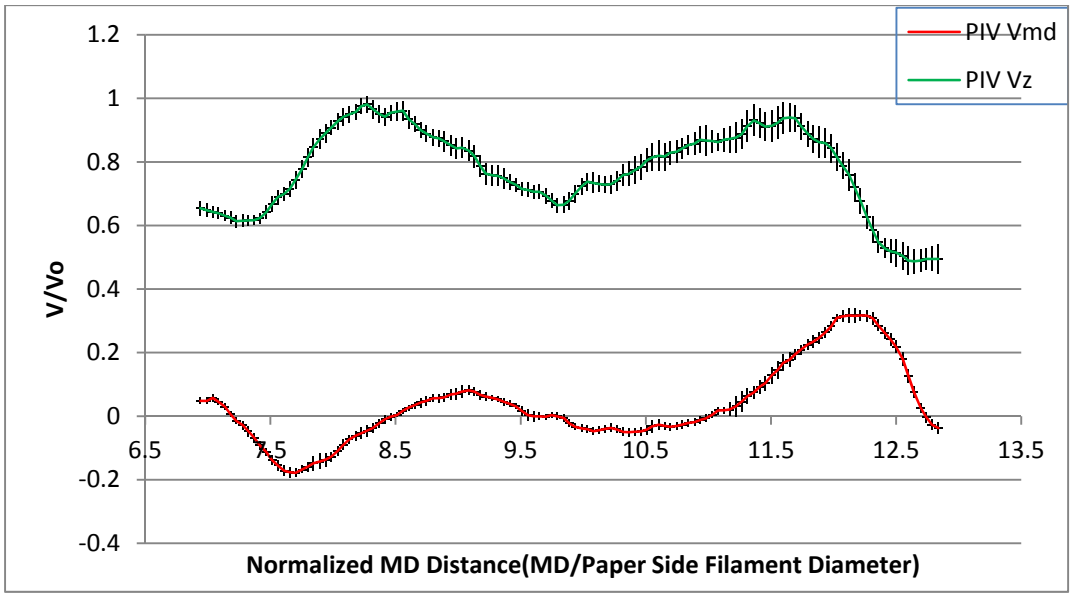


**Figure 4.11 Velocity vs. MD distance, CMD=17cm (11), 0.25d upstream, Re=35**

Figure 4.12 and Figure 4.13 respectively show the ZD and MD velocity contours at a plane 0.25d above the forming fabric. At this plane, the normalized ZD and MD velocity deviations are 19.6% and 14.5%, respectively.

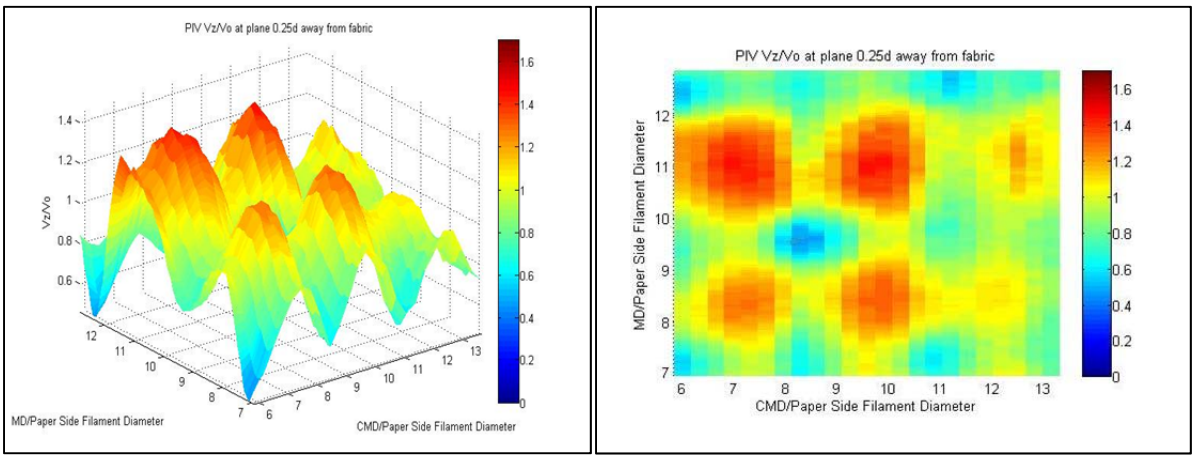


(a) Isometric view (b) Top view

**Figure 4.12 ZD velocity contours in MD velocity setup**

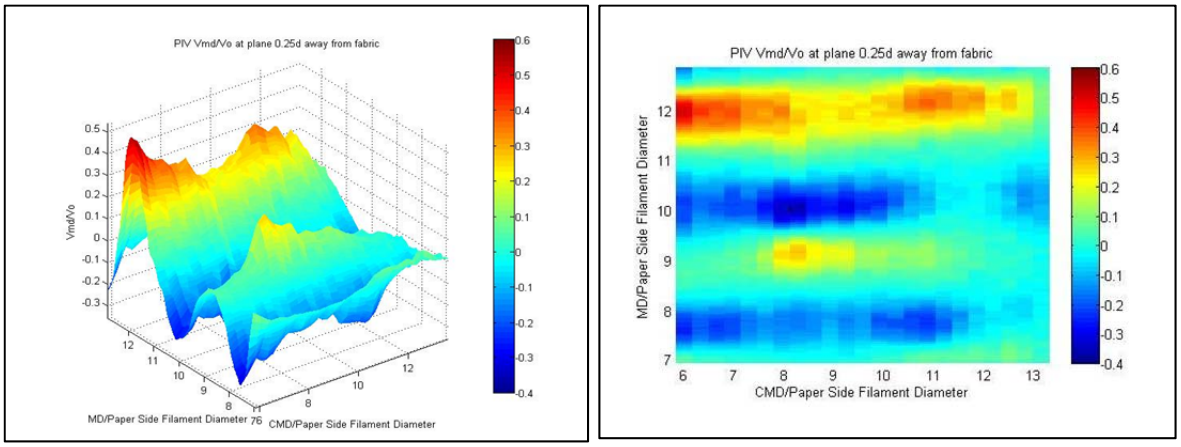


(a) Isometric view (b) Top view

**Figure 4.13 MD velocity contours in MD velocity setup**

Figure 4.14 shows that the normalized ZD and MD velocity deviations decrease from 19.6% to 3.1% and 14.5% to 2.3%, respectively, when the distance to the paper side surface of the

forming fabric increases from 0.25d to 1.5d. Figure 4.15 shows that the highest ZD velocity is about 3.2 times greater than the lowest ZD velocity at a plane 0.25d above the fabric. This value decreases to 1.2 when the distance increases to 1.5d. Figure 4.16 compares the ZD velocity contours between planes 0.25d and 1.5d upstream from the fabric. The figure clearly shows that the velocity contour is nearly uniform at the 1.5d plane, which is also the case for the MD velocity, according to Figure 4.17. The results from Figure 4.14 to Figure 4.17 demonstrate that the non-uniformity caused by the fabric woven structure is only significant within a limited range, i.e. 1.5d above the fabric top surface.

Due to the uncertainty of PIV measurements, which will be described in section 4.3.4, the velocity deviation (e.g. Figure 4.14) will always be larger than zero, and the maximum/minimum ZD velocity in Figure 4.15 will be always larger than one, even very far from the fabric. For the same reason, the contours in Figure 4.16 and Figure 4.17 will never achieve perfect uniformity. The near constancy of the velocity standard deviation for 1.5d and 2d plane indicates that the remaining non-uniformity at the 1.5d plane is mainly caused by experimental error rather than the forming fabric's woven structure.

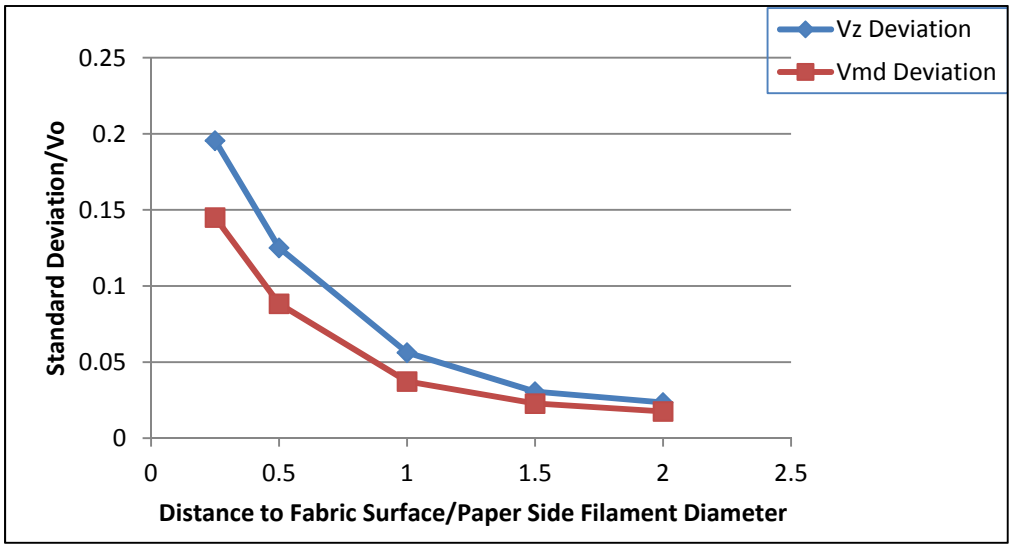


**Figure 4.14 Velocity standard deviation vs. Distance to fabric surface, Re=35, MD velocity setup**

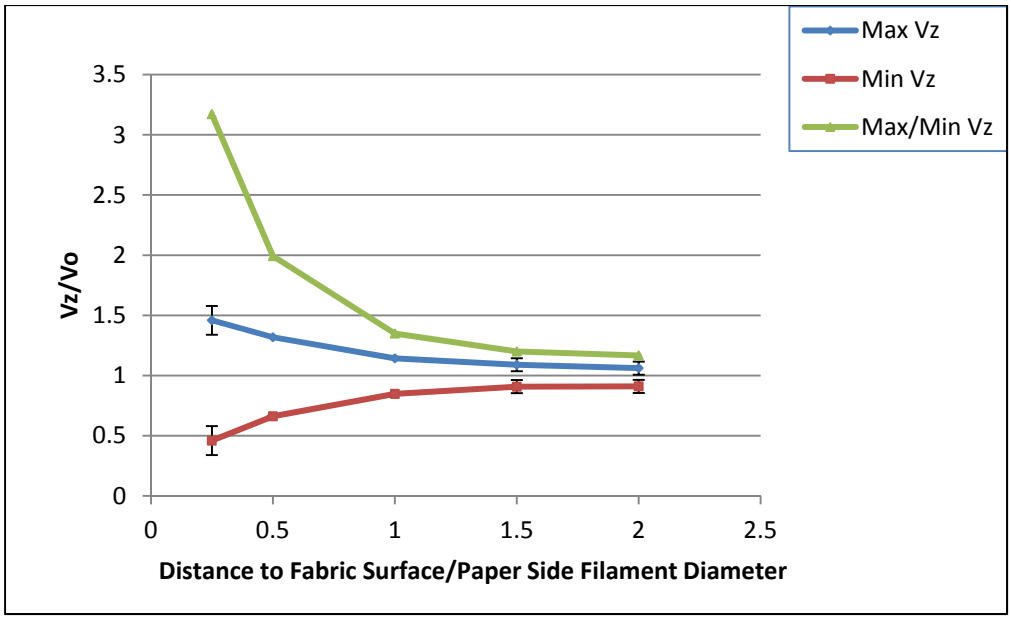


**Figure 4.15 Highest and lowest ZD velocity vs. Distance to fabric surface, Re=35, MD velocity setup**

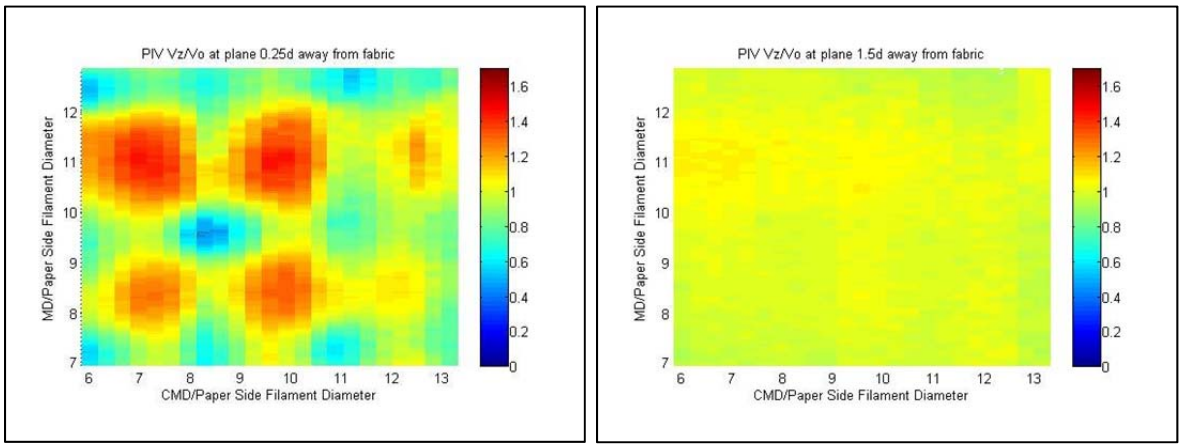


(a) 0.25d upstream (b) 1.5d upstream

**Figure 4.16 ZD velocity contour at different distances to the fabric surface, MD velocity setup**

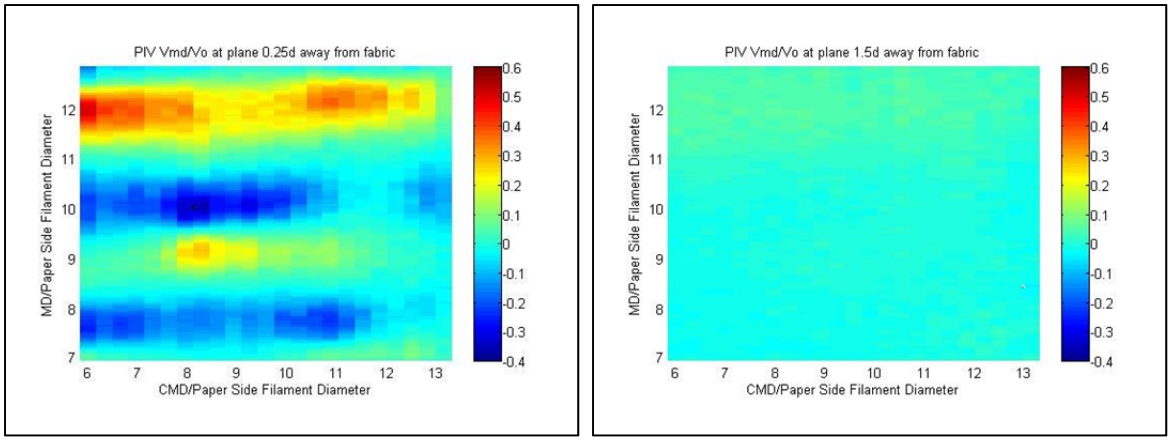


(a) 0.25d upstream (b) 1.5d upstream

**Figure 4.17 MD velocity contour at different distances to the fabric surface, MD velocity setup**

As illustrated in discussions on CMD fiber distributions, here we assume a fiber is oriented in MD, and we average over an MD line with a length equal to the fiber length. With this averaging (Figure 4.18), the velocity non-uniformity in MD is smoothed out when the fiber length equals 0.8mm. The averaging effect would be even greater in real papermaking processes since many wood fibers are longer than 0.8mm and fiber interaction also increases fiber length scale. Although non-uniformity still exists in CMD due to MD filaments, the non-uniformity in CMD will decrease if the fiber is oriented in CMD, as shown in Figure 4.9. Since fibers are oriented randomly in the approach flow, the average velocity contour will be more uniform than the contours shown in Figure 4.18, and in CMD in particular. Figure 4.19 shows that the ratio between the maximum and minimum average ZD velocity over a MD oriented fiber will reduce from 3.2 to 1.5 when the fiber length increases to 0.8mm. For the aforementioned reason, this value of 1.5 will be even closer to one for longer, randomly-oriented fibers, indicating a smoothing out of the velocity non-uniformity. We can therefore

conclude from Figure 4.9, 4.10, 4.18 and 4.19 that fibers that are uniformly distributed in the approach flow will remain so while interacting with this forming fabric.

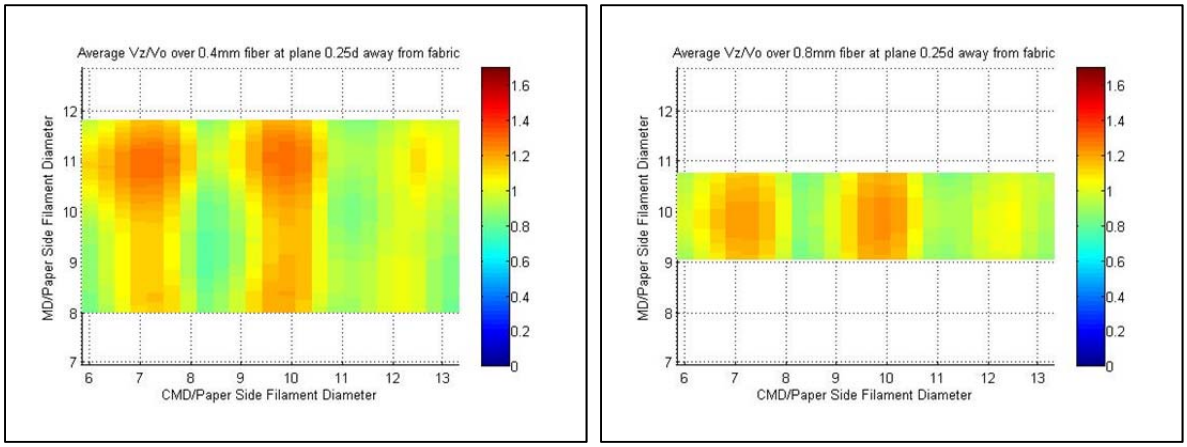


(a) 0.4mm fiber (b) 0.8mm fiber

**Figure 4.18 Contour of average ZD velocity over an MD fiber, 0.25d upstream, Re=35**

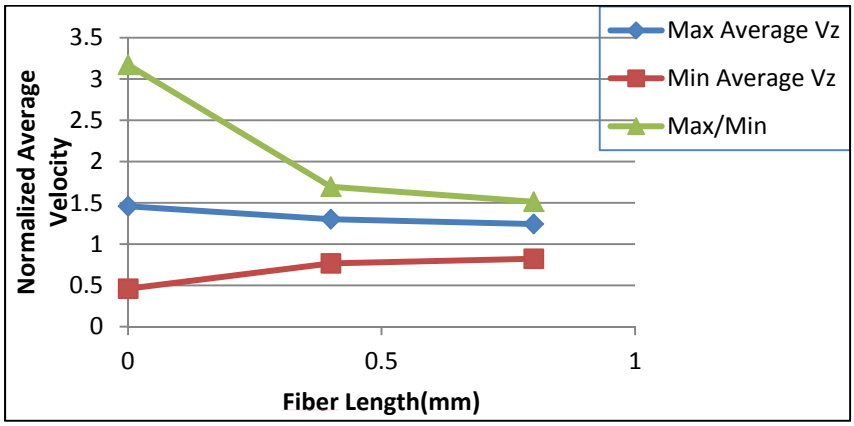


**Figure 4.19 Average ZD velocity over an MD fiber, 0.25d upstream, Re=35**

### 4.3.3 Comparison of Two Orthogonal Measurements of ZD Velocity

The ZD velocity obtained from the MD velocity setup shows similar trends as the ZD velocity results obtained from the CMD velocity setup. Figure 4.20 is a plot of the difference in the ZD velocities of the two orthogonal setups. The structure appeared in this figure (e.g. a vertical oranges stripe at CMD=9.5, and a horizontal blue stripe at MD=11) implies some of

the difference appeared in the figure is due to misregistration, called systematic error in section 4.3.4, of the forming fabric in the two setups. Figure 4.21 shows the RMSE between the ZD velocities obtained from the two orthogonal PIV setups. Each data point in this figure represents the RMSE for all of the data points in one MD line located 0.25d upstream from the forming fabric. The total normalized RMSE, 11.0%, is likely a result of errors in the PIV setup and PIV technique, which will be discussed in the uncertainty analysis section (4.3.4). Even with these errors, the ZD velocity consistency between the two setups is still quite high.

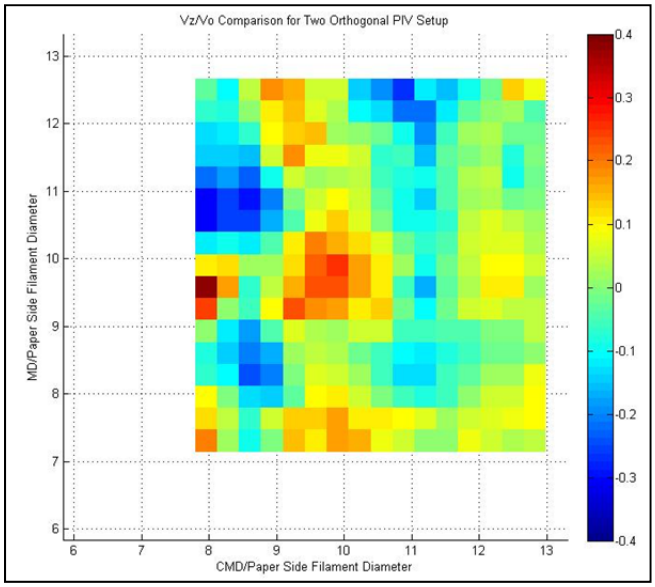


**Figure 4.20 ZD velocity difference between two orthogonal PIV setups, 0.25d upstream, Re=35**

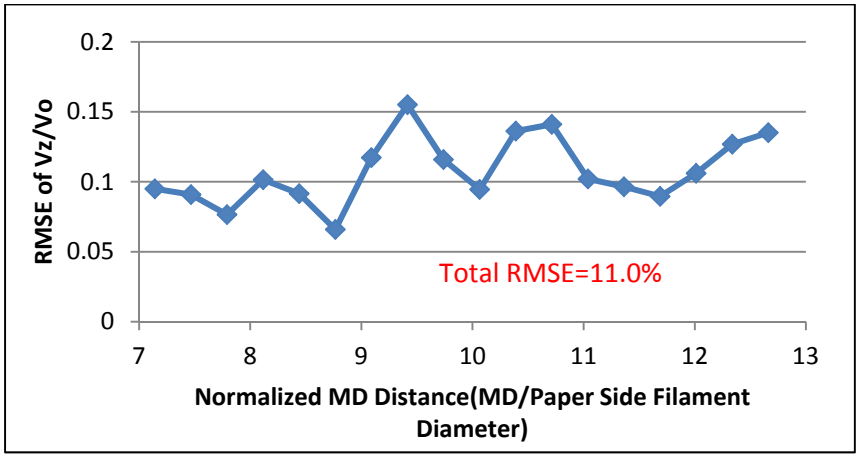


**Figure 4.21 RMSE of ZD velocity between two orthogonal PIV setups, 0.25d upstream, Re=35**

### 4.3.4 Uncertainties of PIV Measurements

The uncertainty of the PIV measurements is mainly caused by two types of errors, PIV technique random error and PIV setup systematic error. The random error represents the PIV technique's precision and has already been described in Figure 4.2 and Figure 4.11, which was calculated by analyzing 30 repetitive measurements over one configuration. With 95% confidence level, in CMD setup, the relative random errors for ZD and CMD velocities are ±7.0% and ±2.8%, respectively; in MD setup, the relative random errors for ZD and MD velocities are ±5.1% and ±3.3%, respectively.

The systematic error of PIV measurements is mainly caused by the misalignment of the fabric model in the test section. Considering the minimum calibration scale in the experiment is 1mm, it has a possible offset of ±0.5mm in three directions, ZD, CMD and MD. Besides, the laser sheet thickness is about 1.5mm, so the position of the laser sheet plane can have a ±1.5mm uncertainty in the laser sheet thickness direction. So the uncertainties of ZD distance, MD distance and CMD distance are as follows.

In CMD setup:

$U_Z$= ±0.5mm, $U_{CMD}$= ±0.5mm, $U_{MD}$=$\sqrt{(\pm 0.5mm)^2 + (\pm 1.5mm)^2} = \pm 1.6mm$

In MD setup:

$U_Z$= ±0.5mm, $U_{CMD}$=$\sqrt{(\pm 0.5mm)^2 + (\pm 1.5mm)^2} = \pm 1.6mm$, $U_{MD}$= ±0.5mm

Since velocity is a function of ZD, CMD and MD position, the systematic uncertainty could be calculated according to the following uncertainty propagation equation:

$$(U_V)_{systematic} = \pm\sqrt{\left(\frac{\partial V}{\partial Z}\right)^2 (U_Z)^2 + \left(\frac{\partial V}{\partial CMD}\right)^2 (U_{CMD})^2 + \left(\frac{\partial V}{\partial MD}\right)^2 (U_{MD})^2}$$

The three derivatives in the above equation could be calculated based on Figure 4.6, 4.7, 4.15 and 4.16.

In CMD setup at 0.25d plane:

$$\frac{\partial V_Z}{\partial Z} = \frac{0.21V_0}{0.25d} = 0.039V_0/\text{mm}$$

$$\frac{\partial V_Z}{\partial CMD} = \frac{\partial V_Z}{\partial MD} = \frac{1.04V_0}{(\frac{310mm}{16})} = 0.054V_0/\text{mm}$$

$$\left(U_{V_Z}\right)_{systematic} = \pm 0.094V_0$$

The systematic uncertainty of CMD velocity is calculated in the same way and the result is:

$$\left(U_{V_{CMD}}\right)_{systematic} = \pm 0.065V_0$$

And for MD setup at 0.25d plane:

$$\left(U_{V_Z}\right)_{systematic} = \pm 0.094V_0$$

$$\left(U_{V_{CMD}}\right)_{systematic} = \pm 0.082V_0$$

The total uncertainty $U_V = \pm\sqrt{(U_V)^2_{systematic} + (U_V)^2_{random}}$, so the 95% confidence intervals of the PIV measurement showed in this thesis are as follows:

In CMD setup at 0.25d plane:

$$U_{V_Z} = \pm 11.7\%V_0$$

$$U_{V_{CMD}} = \pm 7.1\%V_0$$

In MD setup at 0.25d plane:

$$U_{V_Z} = \pm 10.7\%V_0$$

$$U_{V_{MD}} = \pm 8.9\%V_0$$

With the same method mentioned above, the uncertainties at 1.5d plane are as follows:

In CMD setup at 1.5d plane:

$U_{V_Z} = \pm 7.3\% V_0$

$U_{V_{CMD}} = \pm 3.0\% V_0$

In MD setup at 1.5d plane:

$U_{V_Z} = \pm 5.4\% V_0$

$U_{V_{MD}} = \pm 3.6\% V_0$

To summarize, in CMD setup at 0.25d plane, the relative uncertainties of ZD and CMD velocities with 95% confidence intervals are $\pm 11.7\%$ and $\pm 7.1\%$, respectively; in MD setup at 0.25d plane, the relative uncertainties of ZD and MD velocities with 95% confidence intervals are $\pm 10.7\%$ and $\pm 8.9\%$, respectively; in CMD setup at 1.5d plane, the relative uncertainties of ZD and CMD velocities with 95% confidence intervals are $\pm 7.3\%$ and $\pm 3.0\%$, respectively; in MD setup at 1.5d plane, the relative uncertainties of ZD and MD velocities with 95% confidence intervals are $\pm 5.4\%$ and $\pm 3.6\%$, respectively.

## 4.4 CFD Simulation Results and Comparison with PIV Results

### 4.4.1 CAD Model

Vakil et al. [23] developed a new method for creating accurate three dimensional CAD models of forming fabrics. To produce the scale fabric model used in this experiment, we imported this CAD model into a Rapid Prototype Machine. Due to the Rapid Prototype Machine limitations, however, the model had to be divided into four pieces, manufactured separately, and then glued back together, shown in Figure 4.22. This procedure most certainly introduced errors into the geometry of the model. Since a 1º inclination of any part of the model may cause a 0.25d offset, even slight errors will severely affect the PIV result.

In order to ensure that the CAD model was perfectly consistent with the experimental model in the test section, we used a coordinate measuring machine (CMM), located at the University of British Columbia's Manufacturing Automation Laboratory, to measure the coordinates of the experimental model. We then adjusted the CAD model according to the CMM measurements, imported this new CAD model into GAMBIT for meshing, and then to FLUENT™ for simulation.

Owing to the geometry, the CMM result for parts 1 and 2 will be relatively more accurate based on Origin 1, and the CMM results for parts 3 and 4 will be relatively more accurate based on Origin 2. Thus, the angle between part 1 and part 2 was calculated based on Origin 1, and the angle between part 3 and part 4 was calculated based on Origin 2. The angle between the top and bottom half of the fabric was calculated based on Origin 2, since the fabric's bottom plane always touches the frame due to gravity.

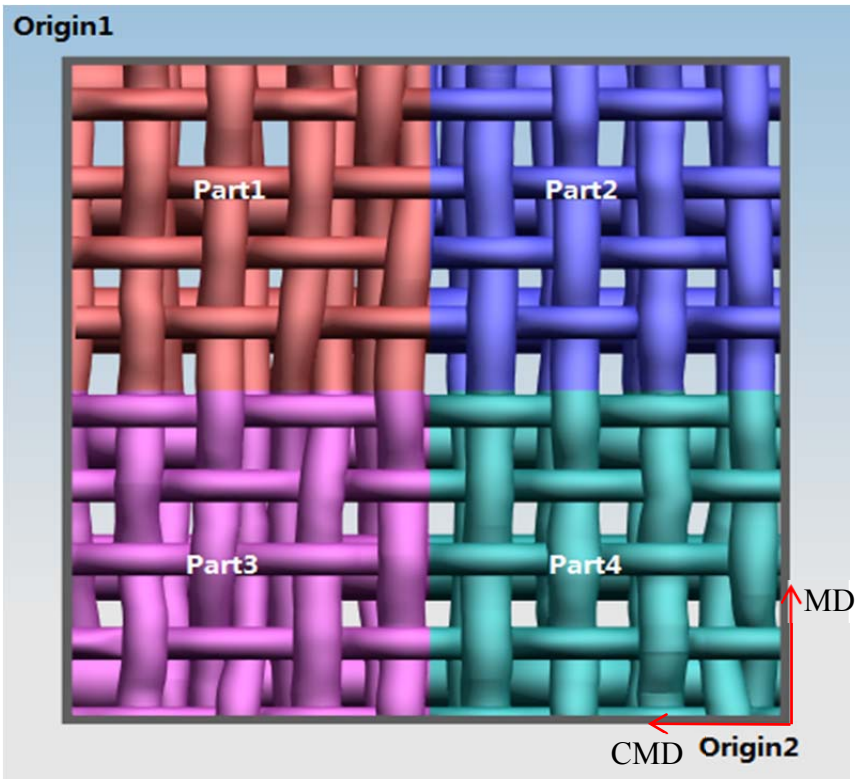


**Figure 4.22 Original CAD model**

Figure 4.23 shows the points measured by CMM based on Origin 1, and Figure 4.24 shows the measurement points based on Origin 2. Most of the measurement points are the local high points on the MD or CMD filaments. To avoid confusion, Origin 1 and Origin 2 have their own coordinate system as shown in Figure 4.23 and Figure 4.24, respectively.

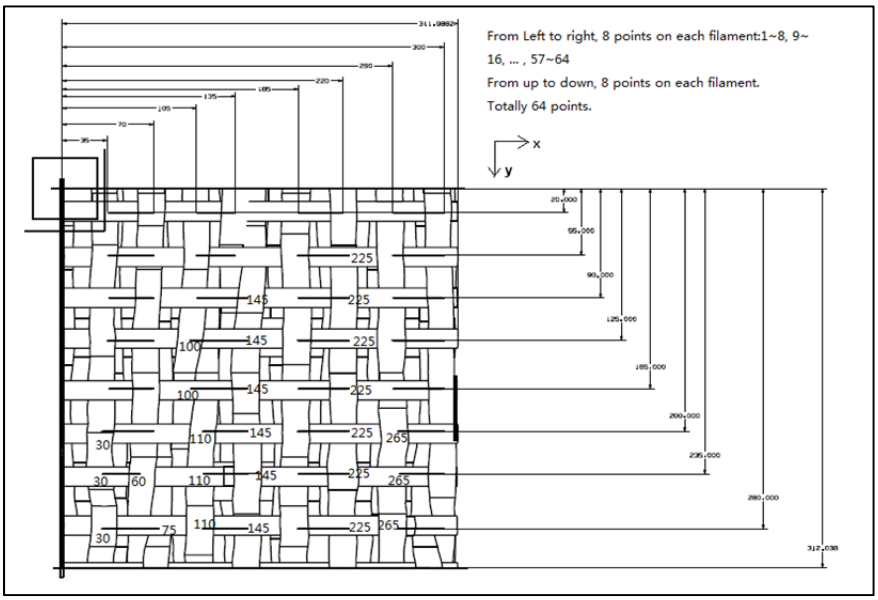


**Figure 4.23 CMM measurement points based on Origin 1**

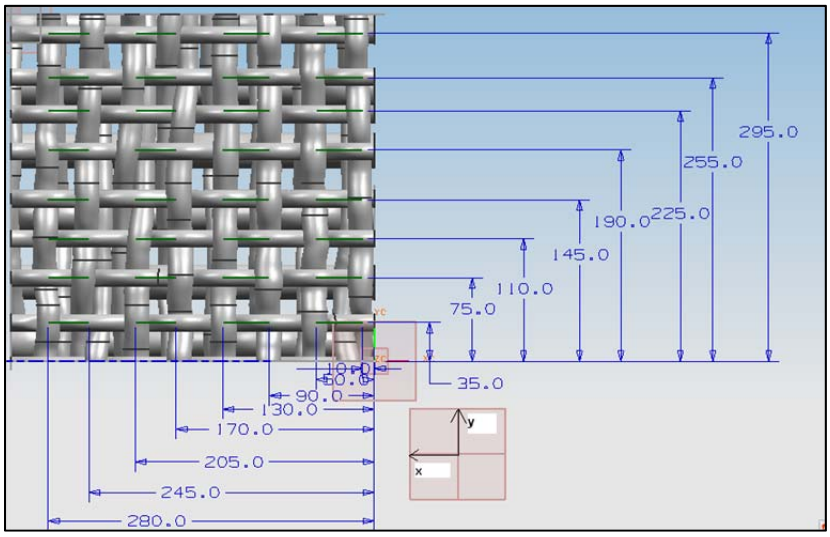


**Figure 4.24 CMM measurement points based on Origin 2**

Figure 4.25 shows the difference between the experimental model and the CAD model based on Origin 1. The difference ranges within (-4.84, 0.11) mm. The maximum difference is more than 4mm which is larger than d/4. The figure clearly shows that there is an inclination angle between part 1 and part 2. To calculate this angle, we average the difference of the four points located on each filament shared by parts 1 and 2 as shown in Figure 4.26. A least squares fit is then applied to the data to calculate the inclination angle between part 1 and part 2: Inclination angle between part 1 and part 2= arctan (-0.0141)= $-0.8^{\circ}$

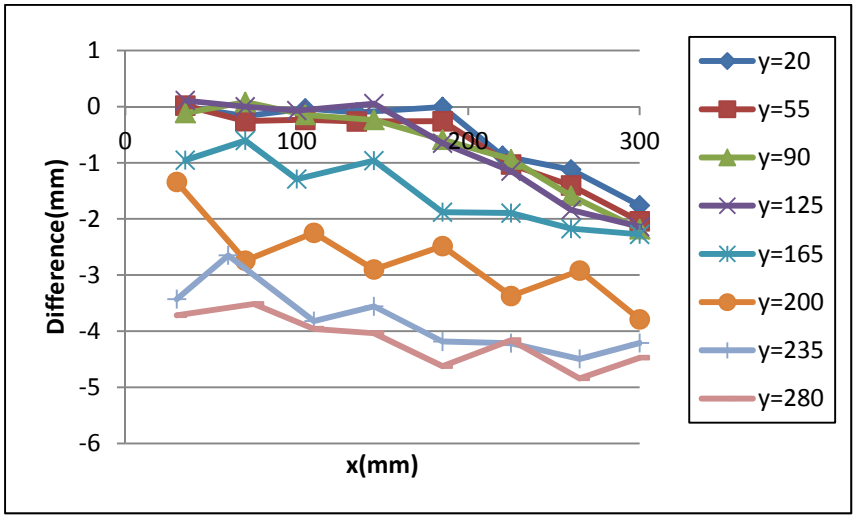


**Figure 4.25 Coordinate difference between experimental model and CAD model based on Origin 1**

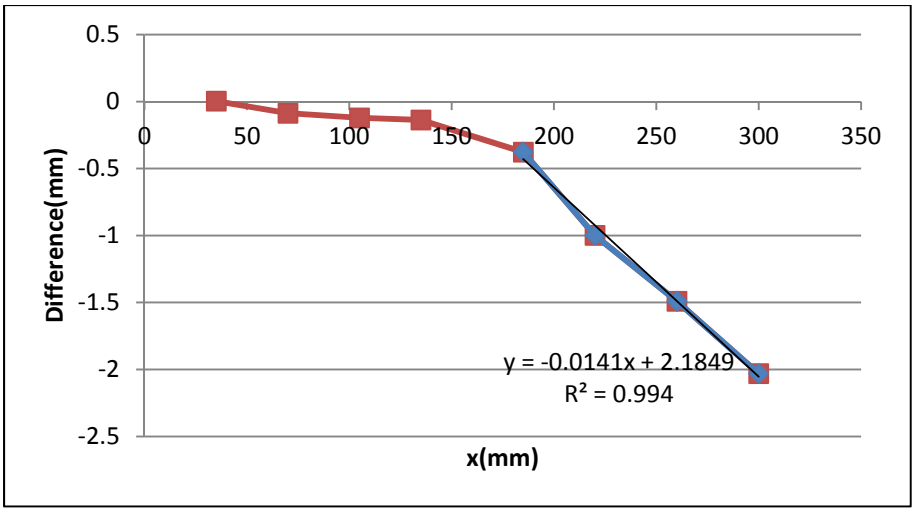


**Figure 4.26 Average difference over each half y direction filament on part 1 and part 2 vs. x, Origin 1**

Figure 4.27 shows the difference between the experimental model and the CAD model based on Origin 2. The difference ranges within (-4.15, 0.019) mm. The maximum difference is also larger than 4mm which is larger than d/4. To calculate the inclination angle between part 3 and part 4, we average the difference of the four points located on each filament shared by parts 3 and 4 as shown in Figure 4.28. The figure clearly shows that inclination and offset between parts 3 and 4 are negligible.

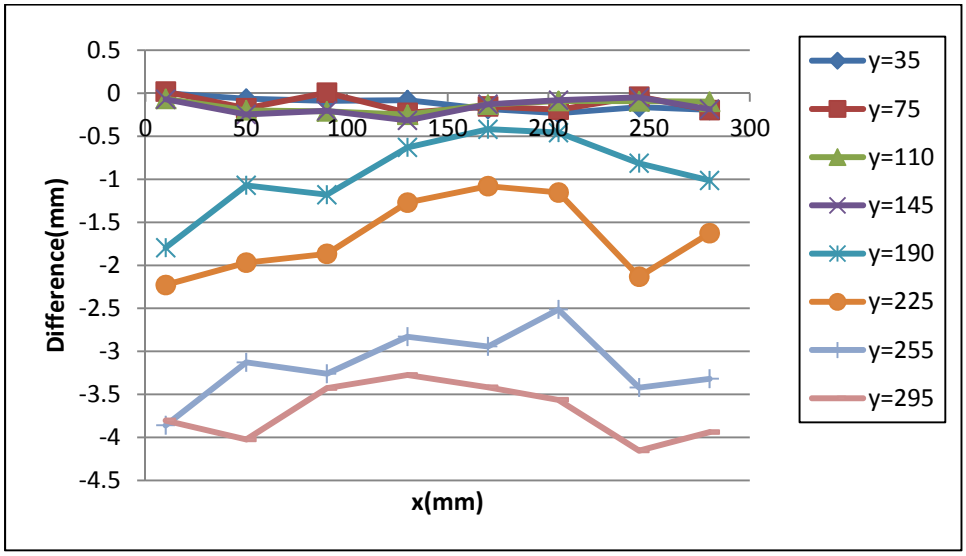


**Figure 4.27 Coordinate difference between experimental model and CAD model based on Origin 2**

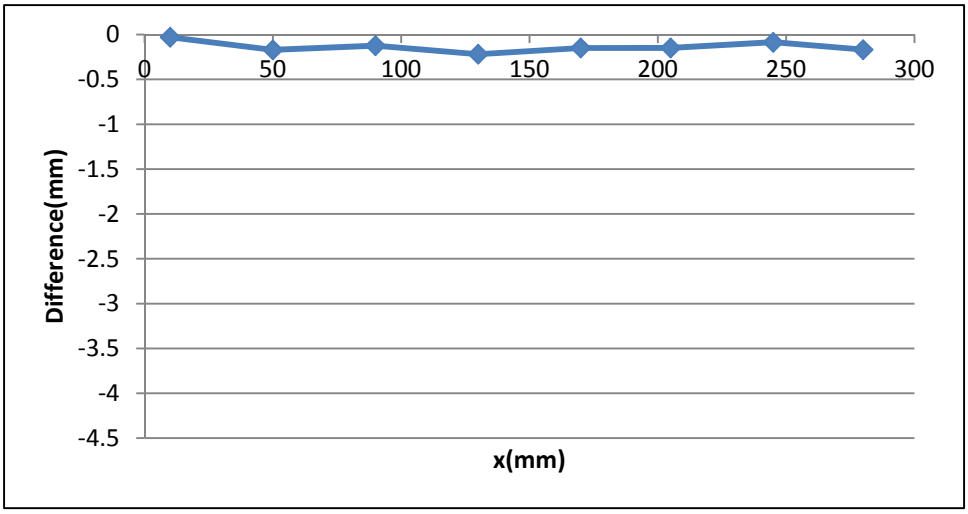


**Figure 4.28 Average difference over each half y direction filament on part 3 and part 4 vs. x, Origin 2**

To calculate the inclination angle between the top (part 1 and part 2) and bottom (part 3 and part 4) halves of the fabric, we average the difference of the 8 points located on each x direction filament, shown in Figure 4.29. The least squares fit shows that the angle is:

Inclination angle between top half fabric and bottom half fabric= $\arctan(-0.0281) = -1.6^{\circ}$

According to the angles calculated above, the CAD model was adjusted using the following steps in Unigraphics NX3:

Step 1: Top half (parts 1 and 2) rotate forward 1.6º with rotation axis parallel to CMD;

Step 2: Part 2 rotate forward 0.8º with rotation axis parallel to MD.

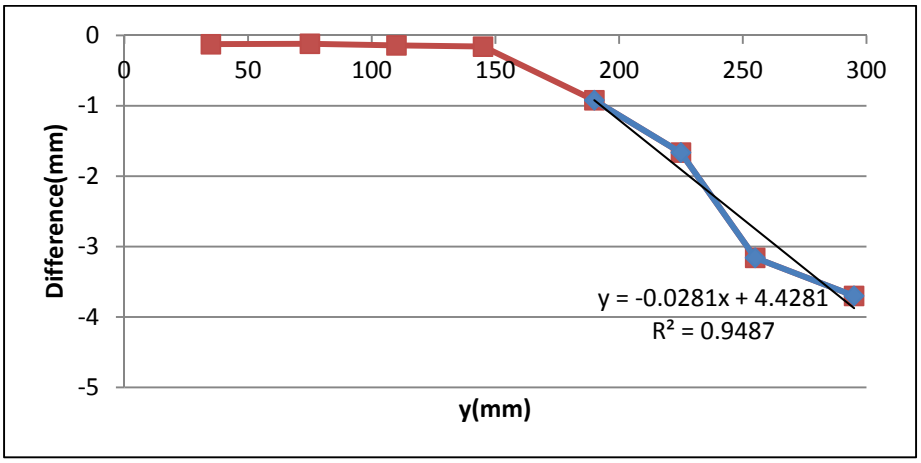


**Figure 4.29. Average difference over x direction filament vs. y, Origin 2**

After the remodelling, the updated difference between the experimental model and adjusted CAD model was plotted in Figure 4.30. The maximum difference reduces from 4.15mm to 1.13mm which is desirable. However, because we can still see an offset of part 2 and an inclination angle of part 1, using a similar method as the one described above, we adjusted the CAD model through two additional steps (Steps 3 and 4) as follows:

Step 3: Part 2 move back 0.8mm in z direction;

Step 4: Part 1 rotate back 0.5º with rotation axis parallel to MD.

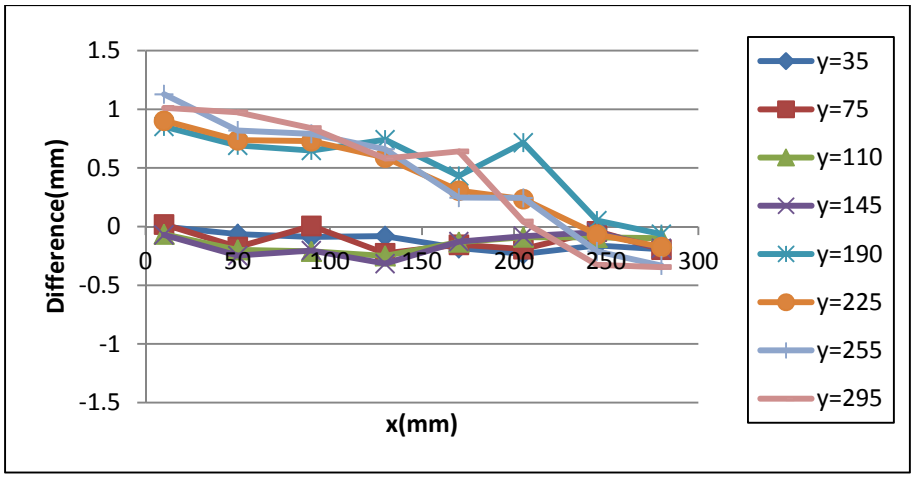


**Figure 4.30 Coordinate difference between experimental model and 2-step adjusted CAD model based on Origin 2**

After Steps 3 and 4 was completed, the new difference was plotted in Figure 4.31, which ranges within (-0.41, 0.33) mm. The highest difference 0.41mm is less than $\frac{1}{37}$d (d is the paper side filament diameter), and thus its effect on flow velocity is negligible. This new CAD model is thus suitable to use for meshing in GAMBIT, simulation in FLUENT™ and finally for comparison with PIV experimental results.

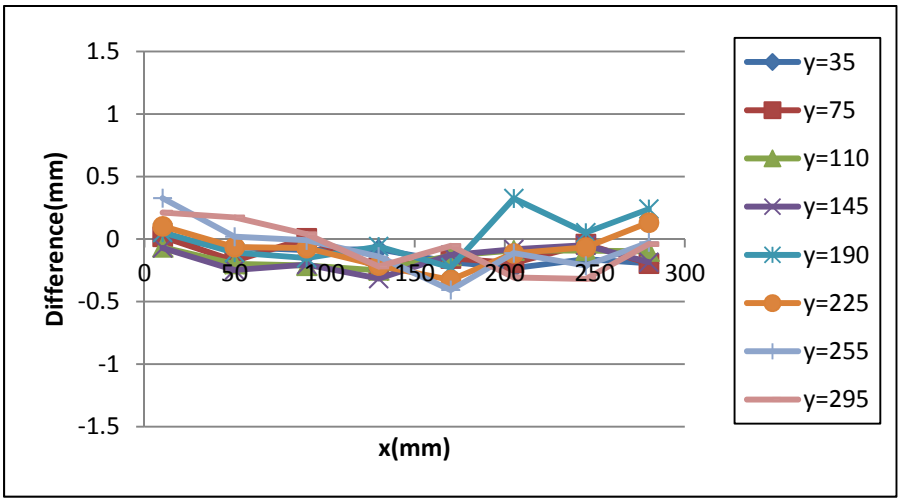


**Figure 4.31 Coordinate difference between experimental model and 4-step adjusted CAD model based on Origin 2**

### 4.4.2 Meshing and Boundary Conditions

Figure 4.32 shows the 3D computational domain and boundary conditions of the flow through the forming fabric. Inlet and outlet boundary conditions are set as Velocity Inlet and Pressure Outlet, respectively. Other surfaces use a No-Slip Wall as a boundary condition. The domain was divided into three parts: Inlet Volume, Fabric Volume and Outlet Volume. The fabric volume was meshed with finer, unstructured tetrahedral/hybrid volume elements. The Inlet Volume and Outlet Volume were meshed with structured hex volume elements to save computational time. A cross section of the mesh is shown in Figure 4.33.

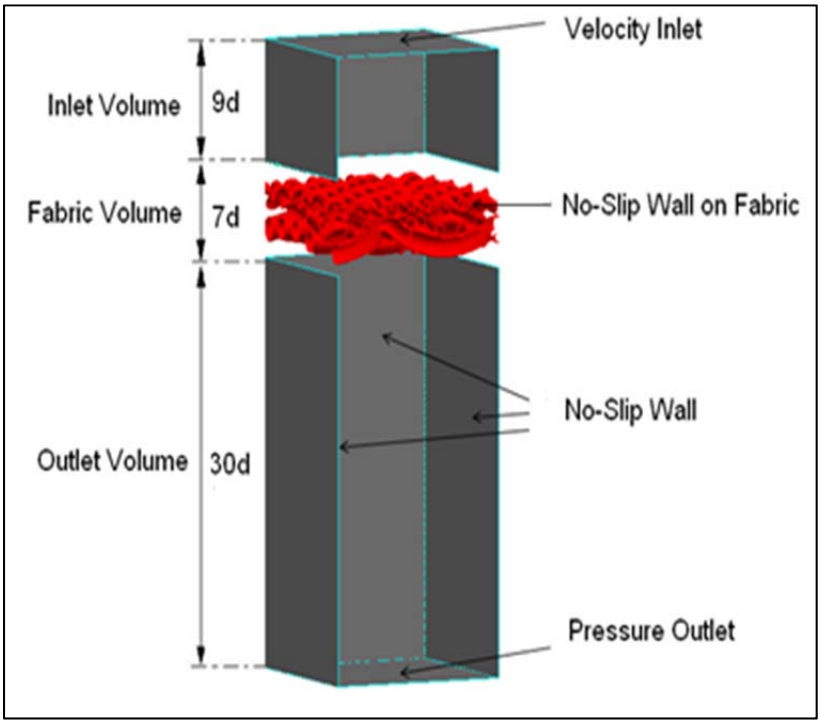


**Figure 4.32 Computational field of the flow through forming fabric**

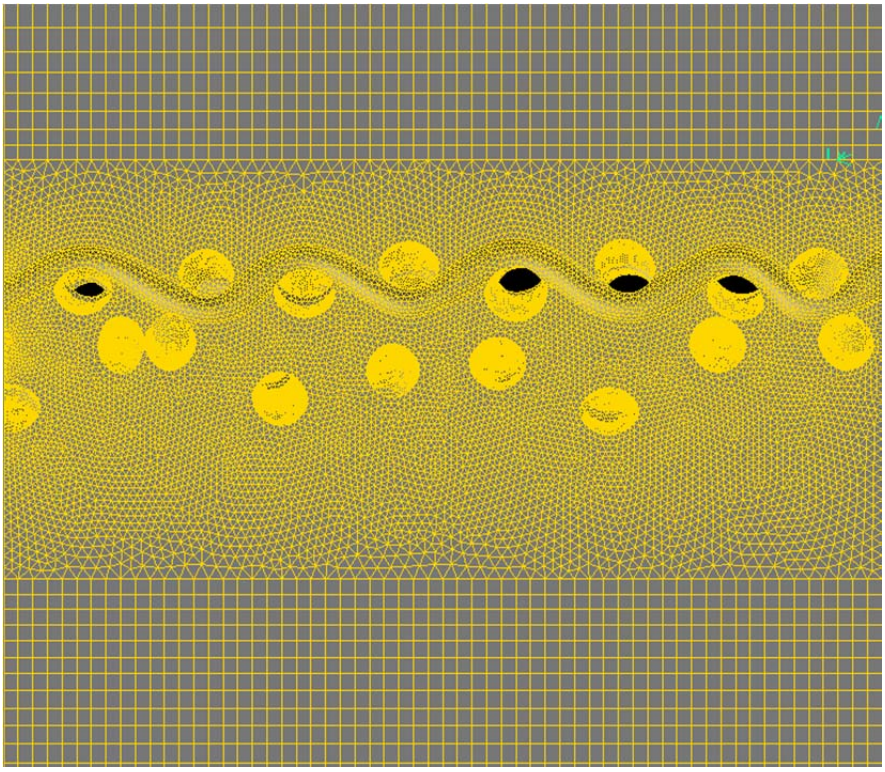

**Figure 4.33 Computational mesh scheme**

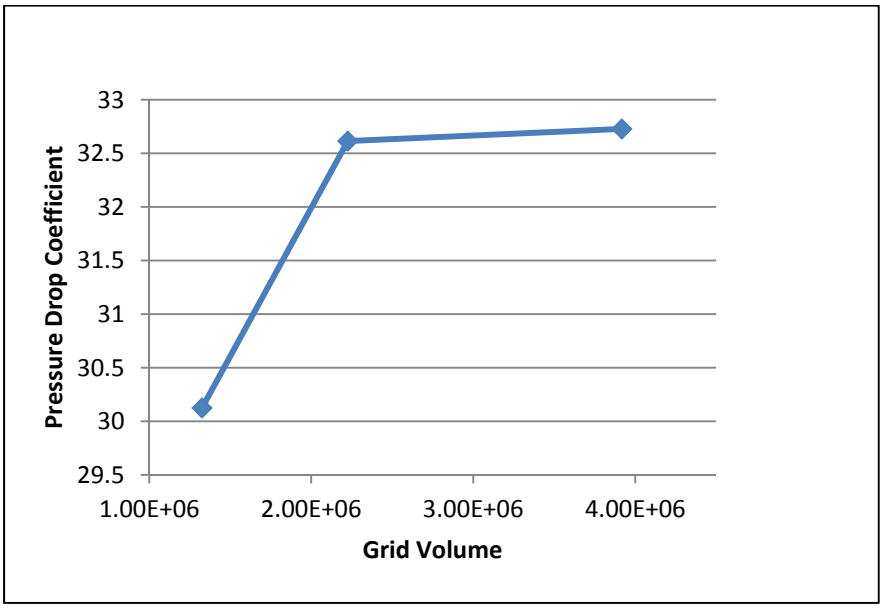


**Figure 4.34 Area weighted average pressure drop against mesh density for Re=35**

The CFD simulations were run with meshes of different density to make sure the results are mesh independent. We conducted simulations of the same fabric model by gradually refining the mesh. Figure 4.34 shows the area weighted average pressure drop coefficient between inlet and outlet as a function of grid volume. Simulations were run at Reynolds number=35. The average pressure drop coefficient on a mesh with 2.2 million cells differs by less than 0.35% from the pressure drop coefficient computed with 3.9 million cells. Therefore, all the simulation results reported in this thesis were run on a grid with approximately 2.2 million cells.

Simulations run at different Reynolds numbers ranging from 15 to 65 showed the same qualitative trends. To provide a comparison with the PIV results shown in the above, all the simulation results were based on Re=35. A three-dimensional steady laminar model was used in FLUENT™.

Using the uncertainty estimation procedure from the Fluids Engineering Division of the ASME, Celik, I. B. et al. [24], the fine-grid convergence index, i.e. discretization error, for this simulation is 0.49%.

### 4.4.3 Comparison of Simulation and PIV Results

Figure 4.35 shows a ZD velocity contour comparison between the simulation and PIV results with the CMD velocity setup. The two contours clearly show the same trends both qualitatively and quantitatively. Figure 4.36 shows the difference between each data point in detail. The difference contour distributes in a structured pattern rather than in random way. This is caused by misalignment of the PIV forming fabric model in the test section. The same

phenomena happen in Figure 4.38, 4.41 and 4.43 because of the same reason. The uncertainties caused by this misalignment have been calculated in section 4.3.4.

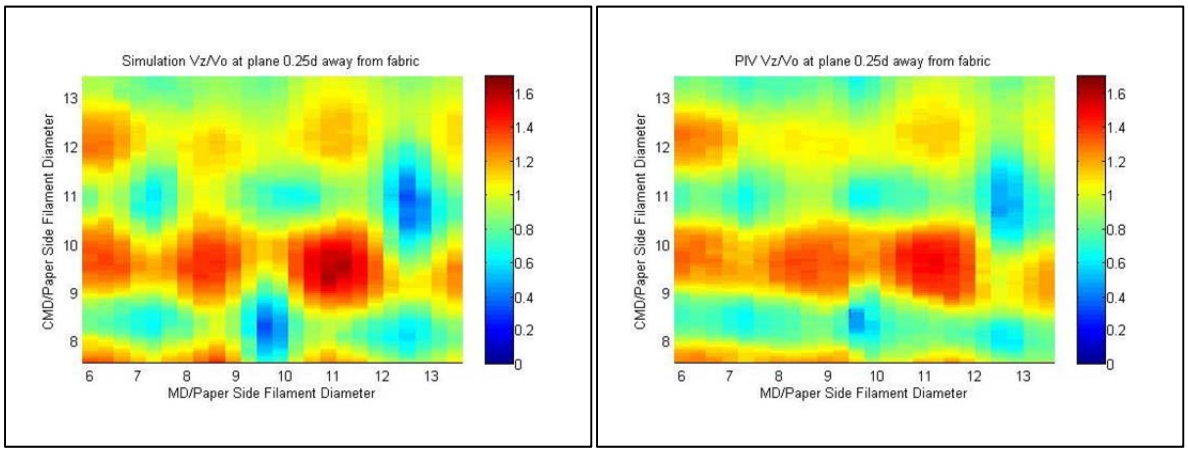


(a) Simulation (b) PIV

**Figure 4.35 ZD velocity contour comparison between simulation and PIV in CMD velocity setup**

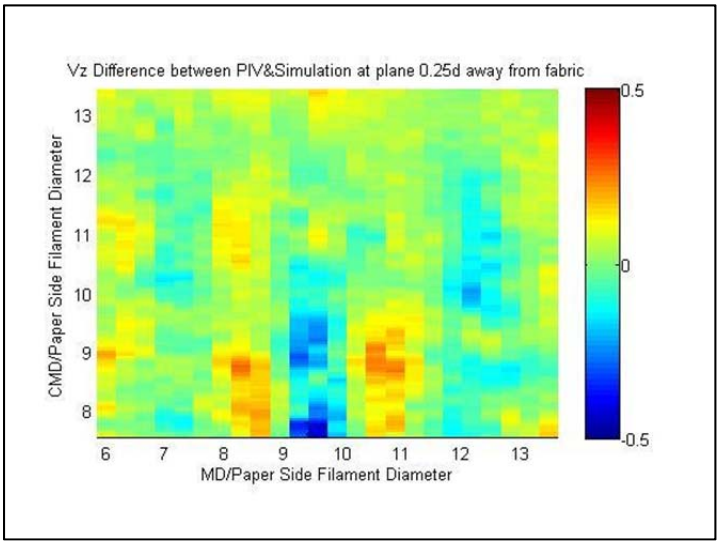


**Figure 4.36 ZD velocity difference between simulation and PIV in CMD velocity setup**

Figure 4.37 shows the CMD velocity contour comparison between the simulation and PIV with the CMD velocity setup. The two contours clearly show the same trend both

qualitatively and quantitatively. Figure 4.38 shows the difference between each data point in detail.

Figure 4.39 shows the RMSE for the data on each measurement plane, which is normal to MD. The total normalized RMSE for ZD and CMD velocities are 8.2% and 4.3% respectively. Since the PIV measurements relative uncertainties for ZD and CMD velocities with the CMD velocity setup are ±11.7% and ±7.1% respectively, the simulation results for ZD and CMD velocities are in the bound of PIV measurement result in CMD velocity setup.

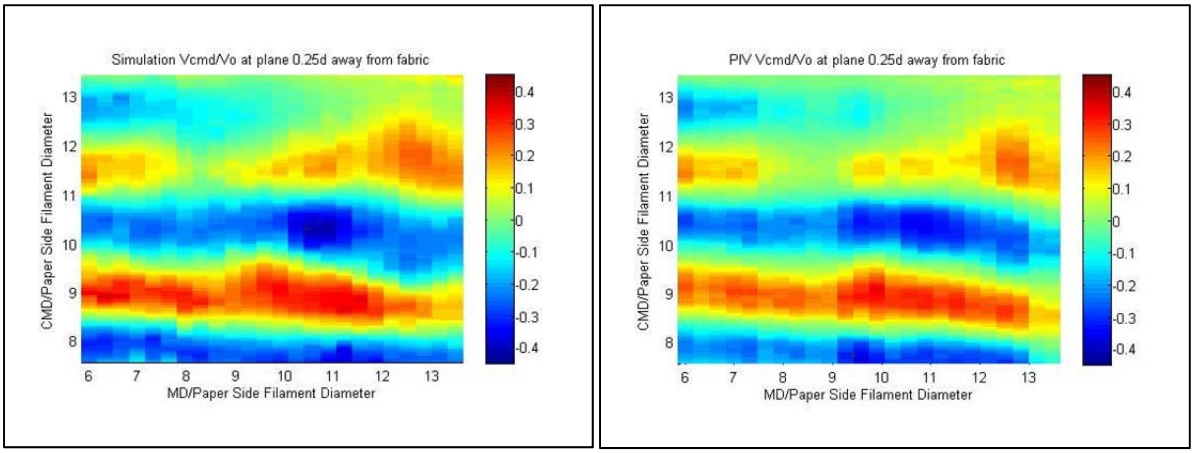


(a) Simulation (b) PIV

**Figure 4.37 CMD velocity contour comparison between simulation and PIV in CMD velocity setup**

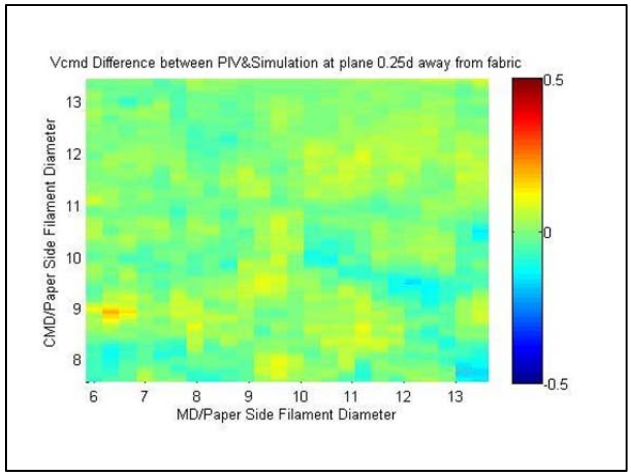


**Figure 4.38 CMD velocity difference between simulation and PIV in CMD velocity setup**

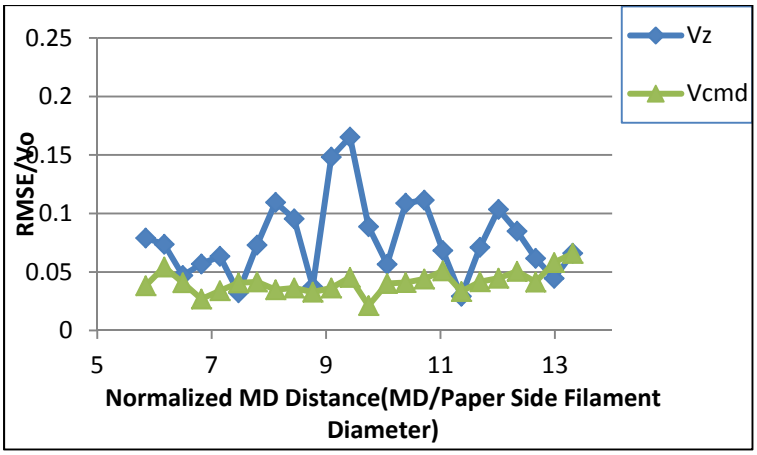


**Figure 4.39 RMSE of the difference between simulation and PIV in CMD velocity setup**

Figure 4.40 shows the ZD velocity contour comparison between the simulation and PIV with MD velocity setup. The two contours clearly show the same trend both qualitatively and quantitatively. To compare in detail, the difference between each data point is shown in Figure 4.41. The structured pattern in this figure is caused by the misalignment of the fabric model in the test section. The uncertainties caused by this misalignment have been calculated in section 4.3.4.

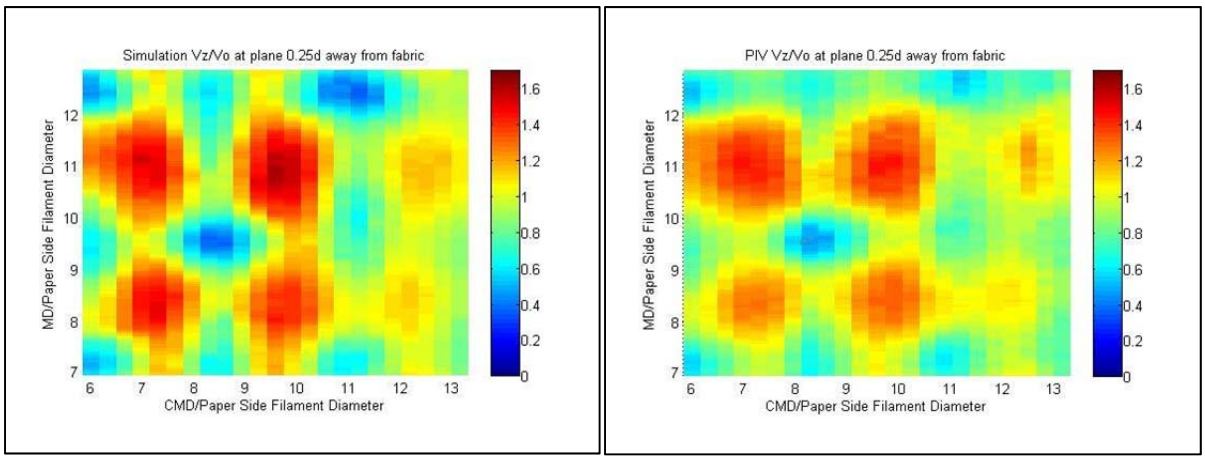


(a) Simulation (b) PIV

**Figure 4.40 ZD velocity contour comparison between simulation and PIV in MD velocity setup**

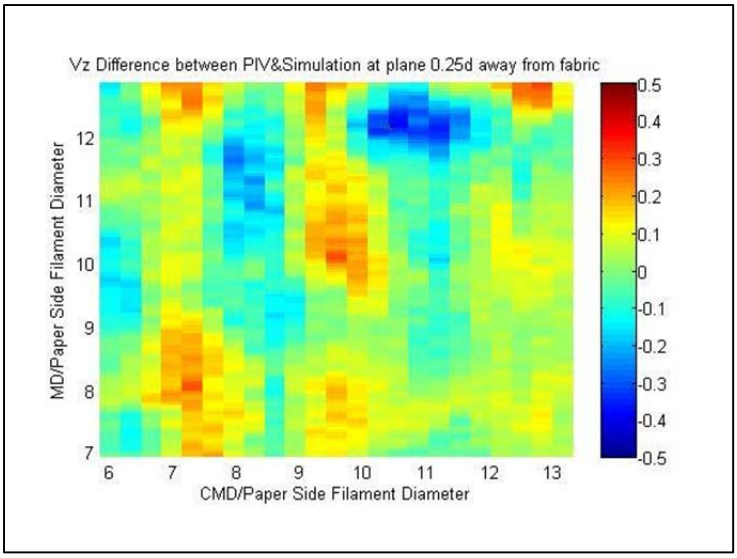


**Figure 4.41 ZD velocity difference between simulation and PIV in MD velocity setup**

Figure 4.42 shows the MD velocity contour comparison between the simulation and PIV with MD velocity setup. The two contours clearly show the same trend both qualitatively and quantitatively. For a detailed comparison, the difference between each data point is shown in Figure 4.43.

Figure 4.44 shows the RMSE for the data on each measurement plane, which is normal to CMD. The total normalized ZD and MD velocity RMSE values are 10.5% and 7.0% respectively. Since the PIV measurements relative uncertainties for ZD and MD velocities with the MD velocity setup are ±10.7% and ±8.9% respectively, the simulation results for ZD and MD velocities are in the bound of PIV measurement result in MD velocity setup.

To summarize, the simulation results are in the bound of PIV measurement results and thus are consistent with the PIV measurement results.

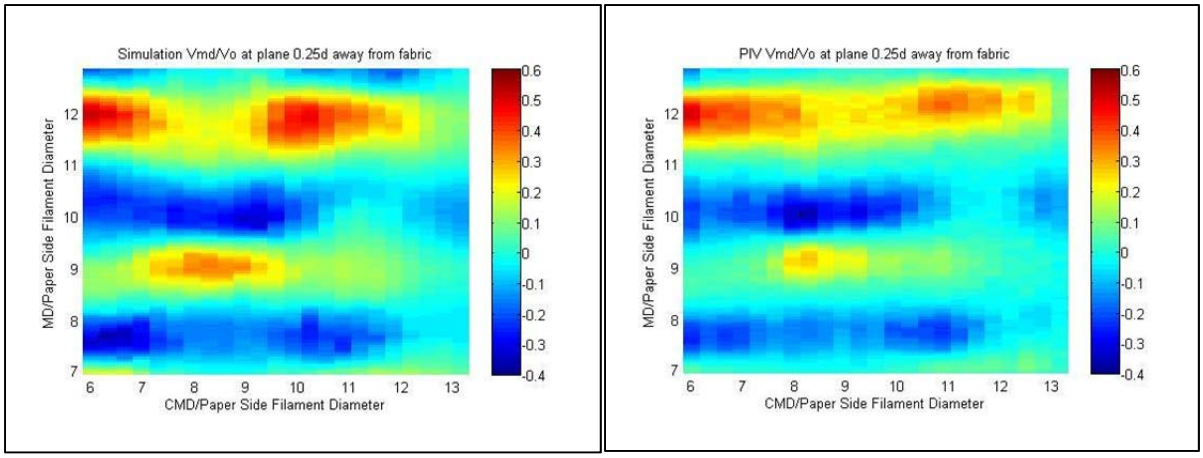


(a) Simulation (b) PIV

**Figure 4.42 MD velocity contour comparison between simulation and PIV in MD velocity setup**

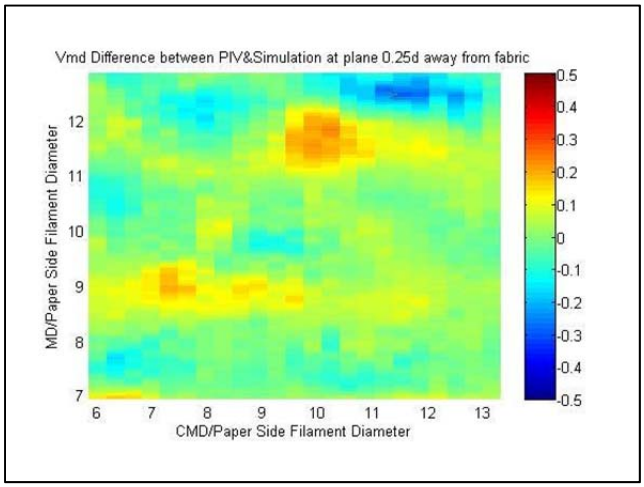


**Figure 4.43 MD velocity difference between simulation and PIV in MD velocity setup**

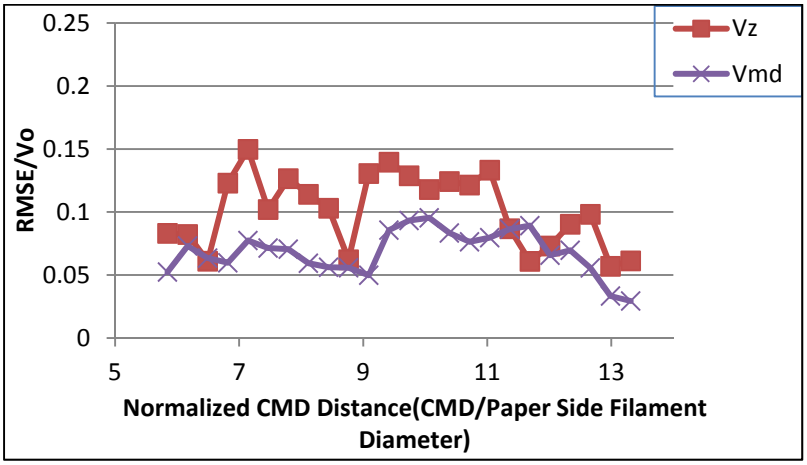


**Figure 4.44 RMSE of the difference between simulation and PIV in MD velocity setup**

## 4.5 Conclusions

PIV measurements of flow through a woven fabric at the Reynolds numbers typical of papermaking have been performed. The measurements show that the normalized ZD velocity deviation decreases from 19.7% at a plane 0.25d upstream from the forming fabric to 4.2% at a plane 1.5d upstream. The normalized CMD velocity deviation decreases from 15.3% at a plane 0.25d upstream from the forming fabric to 1.9% at a plane 1.5d upstream. The normalized MD velocity deviation decreases from 14.5% at a plane 0.25d upstream from the forming fabric to 2.3% at a plane 1.5d upstream. The highest ZD velocity is about 3.3 times higher than the lowest ZD velocity at a plane 0.25d above the fabric. This ratio decreases to 1.2 at a plane 1.5d above the fabric. These findings show that the flow non-uniformity caused by the fabric weave is limited to a short distance above the fabric. However, even this non-uniformity is not particularly felt by fibers, whose length scale results in an averaging of the local velocity field. CFD simulation results of the same flow were consistent with the PIV measurement results.

# Chapter 5: Conclusions

## 5.1 Conclusions

PIV measurements of flow through a woven fabric at the Reynolds numbers typical of papermaking have been performed.

The experiments show that the normalized ZD velocity deviation decreases from 19.7% at a plane 0.25d upstream from the forming fabric to 4.2% at a plane 1.5d upstream. The normalized CMD velocity deviation decreases from 15.3% at a plane 0.25d upstream from the forming fabric to 1.9% at a plane 1.5d upstream. The normalized MD velocity deviation decreases from 14.5% at a plane 0.25d upstream from the forming fabric to 2.3% at a plane 1.5d upstream. The highest ZD velocity is about 3.3 times higher than the lowest ZD velocity at a plane 0.25d above the fabric. This ratio decreases to 1.2 at a plane 1.5d above the fabric. These findings mean that the flow non-uniformity caused by the fabric weave is limited to a short distance above the fabric, i.e. 1.5 times of paper side filament diameter.

However, even this non-uniformity is not particularly felt by fibers, whose length scale results in an averaging of the local velocity field. The fibers distribute uniformly on the fiber mat if they are uniformly distributed in the approach flow.

CFD simulation results of the same flow were consistent with the PIV measurement results. Considering the simulation in this thesis used the similar method proposed by Green et al. [22], the PIV experiment results verifies the simulation method in [22].

This method can be applied industrially to measure velocity distribution in the vicinity of a forming fabric. Velocity distribution causes the localized fiber redistribution in the fiber mat close to the wire side. Because different fabrics possess different velocity distributions, this

factor will have different effects on the fiber distributions of finished paper sheets. With a stronger understanding of velocity distributions in fabrics we can design fabrics that produce superior (more uniform) fiber distribution in finished paper products.

## 5.2 Recommendation for Future Research

The first direction for future research is to use Micro-PIV technique to measure the velocity distribution upstream from the forming fabric. The basic principle of Micro-PIV is the same as regular PIV except the illumination method. For Micro-PIV, the entire test volume will be illuminated rather than only one single plane illuminated in regular PIV. To create a two dimensional plane of viewable particles as regular PIV, Micro-PIV utilizes the ability of the objective lens to focus on only one plane at a time.

One advantage for Micro-PIV is that it can use a real forming fabric for experiments rather than a scale model fabric produced by a rapid prototype machine. This is desirable because the scale model is quite expensive to manufacture.

The other direction for future research is to directly investigate the flow field's effect on fiber distribution by adding fibers into the flow. This could be done computationally or experimentally.

## References

[1]. Adanur, S., 1997. Paper Machine Clothing. Asten, Inc, Basel, Switzerland.

[2]. Danby, R., 1994. The impact of forming fabric structures on print quality. Pulp & Paper Canada, 95(1), 48-51.

[3]. Danby, R., Plouffe, P., 2000. Print quality improvement through forming fabric design changes. Pulp & Paper Canada, 101(9), 66-69.

[4]. Olson, J., 2010. Notes for CHBE 401, Mechanical Pulping and Papermaking.

[5]. Wang, Z., 2006. Numerical simulation of detailed flow through forming fabric. Master's Thesis, The University of British Columbia, Vancouver, British Columbia, Canada

[6]. Johnson, D.B., 1984. Retention and drainage of forming fabrics. Pulp & Paper Canada, 85(6), T167-T172.

[7]. Johnson, D.B., 1986. Retention and drainage of multi-layer fabrics. Pulp & Paper Canada, 87(5), 56-59.

[8]. Paulapuro, H., 2000. Papermaking part 1, Stock Preparation and Wet End. Helsinki, Finland.

[9] Helle, T., 1980. Influence of wire structure on sheet forming, Paper Technology and Industry, 123-131.

[10] Helle, T., 1988. Analysis of wire mark in printing paper. Journal of Pulp and Paper Science. 14(4): J91-J95,

[11]. Raffel, M., Willert, C.I., Wereley, S.T., Kompenhans, J., 1998. Particle Image Velocity, Second Edition.

[12] Helle, T., 1978. How forming fabric design affects drainage and release. Pulp and Paper Canada. 79(11):91-98.

[13] Beran, R.L, 1979. The evaluation and selection of forming fabrics. Tappi Journal, 62(4): 39-44.

[14] Danby, R., 1986. The impact of multilayer fabrics on sheet formation and wire mark. Pulp and Paper Canada, 87(6):69-73.

[15] Adanur, S., 1994. Effect of forming fabric structural parameters on sheet properties. Tappi Journal, 77(10):187-195.

[16] Helmer, R.J.N., Covey, G.H., Raverty,W.D., Vanderhoek, N., Tan, G., 2006. Forming fabrics. drainage rates and paper properties. Appita Journal, 59(3):202-206.

[17] Xu, J., Danby, R., Johnson, D., VandeKolk, J., 2009. The effect of center plane resistance on the drainage property of forming fabric. 95th EXFOR and Annual meeting, 343-349.

[18]. Dalpke, B., Kerekes, R., Green, S., 2004. Modeling jet impingement and the initial drainage zone in roll forming. Journal of Pulp and Paper Science 30, 65-70.

[19]. Huang, Z., 2003. Numerical simulation of flow through model paper machine forming fabrics. Master's Thesis, The University of British Columbia, Vancouver, British Columbia, Canada.

[20]. Huang, Z., Olson, J., Kerekes, R., Green, S., 2006. Numerical simulation of the flow around rows of cylinders. Computers & Fluids 35,485-491.

[21]. Gilchrist, S., Green, S., 2009. Experimental investigation of flow through bank of cylinders of varying geometry. Journal of Fluids and Structures 25, 506-518.

[22]. Green, S., Wang, Z., Waung, T., Vakil, A., 2008. Simulation of the flow through woven fabrics. Computer & Fluids 37, 1148-1156.

[23]. Vakil, A., Olyaei, A., Green, S., 2009. Three-dimensional geometry and flow field modeling of forming fabrics. Nordic Pulp and Paper Research Journal. vol.24 no.3, 342-250.

[24]. Celik, I. B., Ghia, U., Roache, P. J., Freitas, C. J., Coleman, H., Raad, P. E., 2008. Procedure for estimation and reporting of uncertainty due to discretization in CFD applications. Journal of Fluids Engineering, Vol. 130, 078001.